40Ar/39Ar dating of high temperature geothermal systems: First attempt on hydrothermally altered pyroxenes from the Saintes archipelago (Lesser Antilles arc, Guadeloupe)

Alexiane Favier, Chrystele Verati, Jean-Marc Lardeaux, Philippe Münch, Christophe Renac, Michel Corsini, François Orange

$^{40}Ar/^{39}Ar$ dating of high temperature geothermal systems: first attempt on hydrothermally altered pyroxenes from the Saintes archipelago (Lesser Antilles arc, Guadeloupe)

Alexiane Favier[1-2-3*a], Chrystele Verati[2*], Jean-Marc Lardeaux[2-4], Philippe Münch[5], Christophe Renac[2], Michel Corsini[2] and François Orange[6]

1: UMR 5243 Géosciences Montpellier, Université des Antilles-CNRS-Université de Montpellier, Campus de Fouillole, 97159 Pointe-à-Pitre Cedex, Guadeloupe, France
2: UMR 7329 Geoazur, Université Côte d'Azur-CNRS-Observatoire de la Côte d'Azur, 250 rue Albert Einstein, Sophia-Antipolis, 06560 Valbonne, France
3 : Université de Lorraine-CNRS-GeoRessources, F-54000, France
4: Czech Geological Survey, Centre for Lithospheric Research, Klárov 3, 118 21 Prague 1, Czech Republic
5: UMR 5243 Géosciences Montpellier, Université de Montpellier-CNRS-Université des Antilles, Campus Triolet CC060, Place Eugène Bataillon, 34095 Montpellier, France
6: Université Côte d'Azur, Centre Commun de Microscopie Appliquée (CCMA), 06108 Nice, France
* corresponding authors (alexiane.favier@univ-lorraine.fr, chrystele.verati@univ-cotedazur.fr)

Abstract

We investigate the potential of ^{40}Ar-^{39}Ar systematics in secondary K-bearing minerals developed at the expense of hydrothermally altered volcanic pyroxenes from a fossil geothermal system located in the Saintes archipelago (Lesser Antilles magmatic arc).
Our work reports the first example of dating hydrothermal muscovite crystallization developed during pseudomorphic transformation of pyroxenes within altered rhyodacites at temperatures above 300°C. The white micas display a well-defined Ar/Ar plateau age of 2.59 ± 0.12 Ma, interpreted as the best age estimate for high temperature fluid circulation in the Saintes geothermal paleo-reservoir. A model of muscovite substitution by illite during cooling supports the interpretation that illitization perturbs the K-Ar and the Ar-Ar ages only when muscovite is highly illitized and/or if illitization is significantly younger than muscovite crystallization. The whole temporal dataset implies a fast cooling rate (>150°C/200 ka) and a maximal lifetime of 650 ka for the Saintes hydrothermal system.

Keywords: $^{40}Ar/^{39}Ar$ dating, fossil geothermal system, hydrothermal reaction, meta-pyroxene, white mica, muscovite, illite

1. Introduction

Tectonic settings favourable for high temperature geothermal energy are mainly located in areas with active volcanism, i.e., subduction, hotspot and rift zones (Arnórsson, **1995**; Bibby *et al.*, **1995**; Sasada *et al.*, **2000**; Ragnarsson, **2015**; Bertani, **2016**; Barcelona *et al.*, **2019**). Although many studies have explored structural, mineralogical, geochemical and geophysical characteristics to constrain the three-dimensional geometry of plumbing systems in active geothermal reservoirs, very few data are available on the duration of geothermal processes in active geothermal systems (Grimes *et al.*, **1998**; Dalrymple *et al.*, **1999**; Arehart *et al.*, **2002**; Villa *et al.*, **2006**; Wilson *et al.*, **2008**; Verati *et al.*, **2014**; Oze *et al.*, **2017**). This lack of data is also true for epithermal systems that are recognized in magmatic arcs and commonly considered to be fossil geothermal systems (Brockamp *et al.*, **2003**; Oliveros *et al.*, **2008**; Hames *et al.*, **2009**; Márton *et al.*, **2010**). Indeed, very few minerals are available for geochronology within the hydrothermally altered domains recognized in geothermal fields

[a] Permanent address : alexianefavier@outlook.com

worldwide. Usually, zircons from hydrothermally altered magmatic rocks are used with U-Pb and U-Th dating methods (Milicich et al., 2020; Rosenberg et al., 2020). Regarding the $^{40}Ar/^{39}Ar$ technique, most analyses attempted to date have been carried out on sericite, adularia, alunite, celadonite and clay minerals (Dong *et al.*, **1995**; WoldeGabriel *et al.*, **1996**; Hall *et al.*, **1997**; Haines & van der Pluijm, **2008**; Oliveros *et al.*, **2008**; Clauer *et al.*, **2012**; Clauer, **2013**; Verati & Jourdan, **2014**; Verati *et al.*, **2014**; Oze *et al.*, **2017**). These minerals suitable for the Ar-Ar method under epithermal conditions are mainly developed at the expense of primary magmatic feldspars. However, feldspars are often completely replaced by clay minerals during supergene alteration (Browne, **1978**; Mas *et al.*, **2006**). Thus, we need to find more dateable mineral systems for such geological conditions.

The aim of this article is to investigate the potential of ^{40}Ar-^{39}Ar systematics in secondary K-bearing minerals developed at the expense of volcanic pyroxenes in relation to high temperature hydrothermal fluid circulation within a fossil geothermal system located in the Lesser Antilles magmatic arc and more precisely in the Saintes archipelago.

This study focuses on the identification of K-bearing phases present in hydrothermally altered pyroxenes, hereafter called “meta-pyroxenes”, in order to decipher whether the Ar-Ar method can be appropriately applied in such a complex microstructure (i.e., pseudomorphic transformation) within which numerous secondary phases could be mixed. Dating the crystallization of minerals replacing volcanic pyroxenes offers a promising and new way to constrain the age and duration of hydro- or geo-thermal systems in subduction-related magmatic arcs.

2. Geological setting and petrological framework

In the active Lesser Antilles arc, the Saintes archipelago represents small volcanic islands (from the largest to the smallest islands: Terre-de-Bas, Terre-de-Haut, and their islets: Îlet à Cabris, Grand îlet and Îlet la Coche; Fig. 1-A and 1-B). These islands, in the framework of the Guadeloupe archipelago, are related to the recent active volcanic arc emplaced since 4.28 Ma (Carlut et al., 2000; Samper et al., 2007; Samper et al., 2009; Ricci et al., 2015a; Ricci et al., 2015b; Ricci et al., 2017; Favier *et al.*, **2019**). The Saintes Islands consist of typical calc-alkaline volcanic rocks, with ages ranging from 2.00 ± 0.03 to 2.98 ± 0.04 Ma for Terre-de-Haut Island and less than 1 Ma for Terre-de-Bas Island (Zami *et al.*, **2014**). Volcanic formations include rhyodacite, dacite and andesite domes and/or lava flows associated with many debris flows and pyroclastic flows (Fig. 1-B).

In recent years, several studies (Verati et al., 2016; Navelot et al., 2018; Beauchamps et al., 2019; Favier et al., 2021) have identified this hydrothermal system as an eroded and exhumed geothermal system. In Terre-de-Haut Island, superposed fault networks are well known since pioneering investigations of Jacques and Maury (1988). In previous papers (Verati et al., 2016; Navelot et al., 2018) we demonstrated that the hydrothermal zone of Terre de Haut was located at a set of two intersecting fault families N090-N110 and N130-N140 delimiting it within a graben-like structure (Figure 1C) in relation to the overall tectonic setting of the volcanic arc (arc-perpendicular extension structures, Feuillet et al. 2002). We also discovered ductile tectonic structures, pressure solution cleavages, concentrated in schistose corridors intersected by the brittle faults (Figure 1 C, Favier et al., 2021). High-temperature hydrothermal phases crystallize in the schistose corridors (Favier et al., 2021) while low-temperature hydrothermal phases are mainly located in fractures, veins and brittle faults (Navelot et al., 2018; Beauchamps et al., 2019; Favier, 2019). At the scale of Terre-de-Haut Island, the finite strain pattern is heterogeneous and consequently the progressive high-temperature hydrothermal transformations of volcanic formations are identifiable from the undeformed, or slightly deformed area, to the most deformed shear zone.

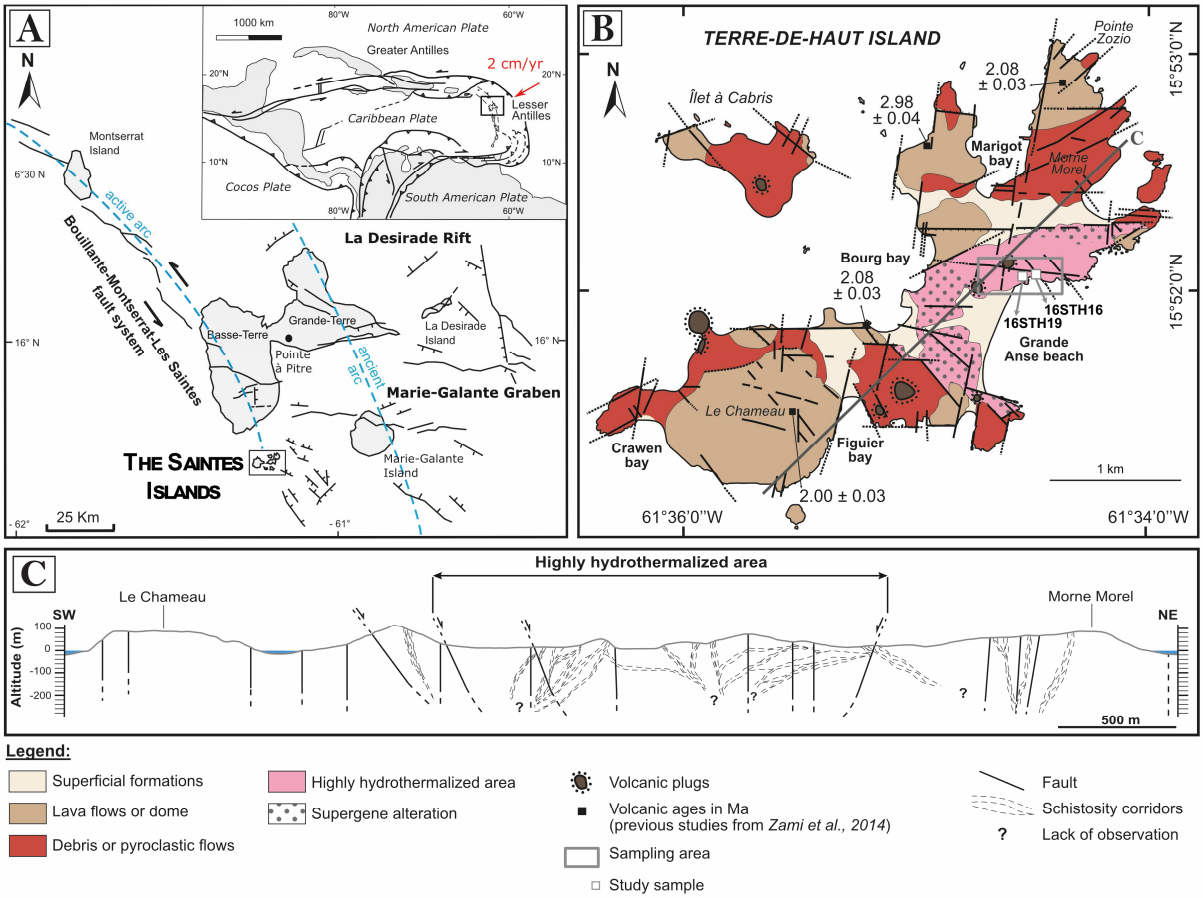

Figure 1: A) Location of the Lesser Antilles arc system and the Saintes archipelago (modified from Bouysse & Westercamp, 1990). The Saintes Islands are located in the inner active arc. B) Geological map of the Saintes archipelago (i.e., Terre-de-Haut and Ilet à Cabris; Terre-de-Bas is not shown). Volcanic K-Ar ages (Zami *et al.*, 2014) are reported. The location of the analysed samples are shown within the highly hydrothermalized area (after Verati *et al.*, 2016; Navelot *et al.*, 2018; Favier, **2019**; Favier *et al.*, **2021**). C) NE-SW cross-section (localization in fig.1-B) from Terre-de-Haut Island displaying the superposition of brittle faults upon the network of schistosity planes. The highly hydrothermalized area is located in the central part of the cross-section within a WNW-ESE graben (modify from Favier et al., 2021). ***[Color]***

Outside of the hydrothermal zone, fresh volcanic rocks display typical porphyritic textures (Fig. 2 A to C and 3-A and B). The chemistry and the number of phenocrysts are variable according to the lithotype of the volcanic rocks; in all samples, the following primary phases are always observed in decreasing order of abundance: plagioclases (mainly labradorites), clinopyroxenes (augites), orthopyroxenes (hypersthenes), amphiboles (hornblende to edenite or pargasite depending on the considered bulk-rock chemistry, Jacques & Maury, **1988**) and Fe-Ti oxides (ilmenite or titanomagnetite). These volcanic rocks also show a volcanic groundmass rich in millimetre-sized microlites, mainly Fe-Ti oxides associated with anorthoclase in dacites and rhyodacites.

In the hydrothermal zone, the volcanic minerals (mainly pyroxene and amphibole) are partially or totally replaced by secondary phases (Fig. 2 D to H), and in the most altered rocks, the primary volcanic mineralogy has been totally erased (Fig. 2-I). However, where the rocks have escaped supergene alteration, the following secondary hydrothermal phases are observed at the rock sample scale (Favier *et al.*, **2021**): albite + chlorite + muscovite + biotite + clinozoisite + epidote + titanite + quartz. This mineral association is typically described in active or fossil geothermal systems worldwide for temperatures ranging between 300 and 380°C (Browne, **1978**; Henley & Ellis, **1983**; Hedenquist & Browne, **1989**; White &

Hedenquist, **1990**; Groves *et al.*, **1998**; Goldfarb *et al.*, **2001**; Cherkose & Mizunaga, **2018**). The occurrence of secondary K-bearing minerals is particularly well developed in hydrothermally altered pyroxenes (i.e., meta-pyroxenes), which suggests that geochronological K-Ar and/or Ar-Ar methods can be applied here to date the hydrothermal activity developed under these temperature conditions.

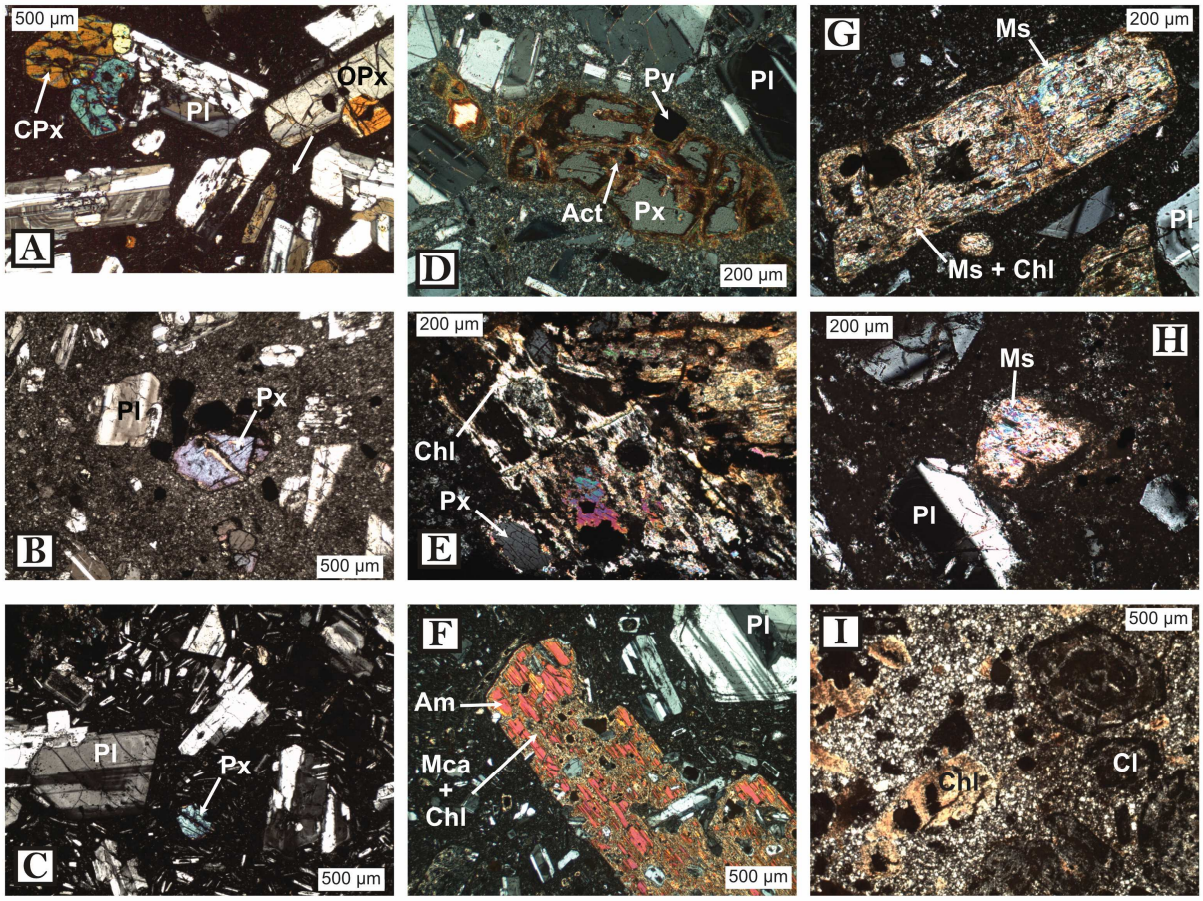

Figure 2: Some examples of volcanic textures found in Terre-de-Haut Island. A) Fresh andesitic lava flow. B) Fesh dacitic lava flow. C) Andesite fragment from pyroclastic flow. D) Altered andesitic lava flow, pyroxene partially replaced. E) Altered dacitic lava flow, volcanic pyroxene partially replaced. F) Altered rhyodacite from a pyroclastic flow, volcanic amphibole partially replaced. G) Volcanic pyroxene totally replaced by white mica and chlorite, in an altered dacite of the highly hydrothermalized area. H) Volcanic pyroxene totally replaced by white mica, in an altered dacite of the highly hydrothermalized area. I) Primary volcanic mineralogy totally erased (plagioclase and pyroxene replaced respectively by clays minerals and chlorite), in a highly altered rhyodacite. Act = actinolite, Am = amphibole, Chl = chlorite, Cl = clay minerals, Mca = mica, Ms = muscovite, Pl = plagioclase, Px = pyroxene (C = clino- and O = ortho-), Py = pyrite.

3. Materials and Methods

After recovering 35 samples in the field from the highly hydrothermalized area of Terre-de-Haut Island (Fig. 1-B, 3-C and D) and based on subsequent preliminary observations of thin sections, we selected two samples (16STH16 and 16STH19) that are not affected by supergene alteration and contain meta-pyroxene crystals developed well enough to perform mineralogical measurements. To carry out further geochronological investigations, we chose sample 16STH19, in which the meta-pyroxenes were the most highly developed. After crushing this rock, we selected the 315-500 µm size fraction representing the apparent meta-pyroxene size distribution in thin section. A series of magnetic separations (Frantz Isodynamic® Separator Model L-1) applied to grains allowed the removal of sulphide and

oxide crystals and the concentration of meta-pyroxenes in the less magnetic aliquot. After HNO_3 leaching (1 N, 70°C) for a few hours to avoid residual oxide or sulphide inclusions, this fraction was repeatedly cleaned with an ultrasonic bath in distilled water, rinsed with ethanol and dried (<50°C). The remaining grains were handpicked under a binocular microscope (Fig. 4). We performed scanning electron microscopy and electron microprobe measurements on thin sections and X-ray diffraction from this separated 315-500 µm fraction to characterize the morphology, mineralogy and chemistry of these meta-pyroxene grains.

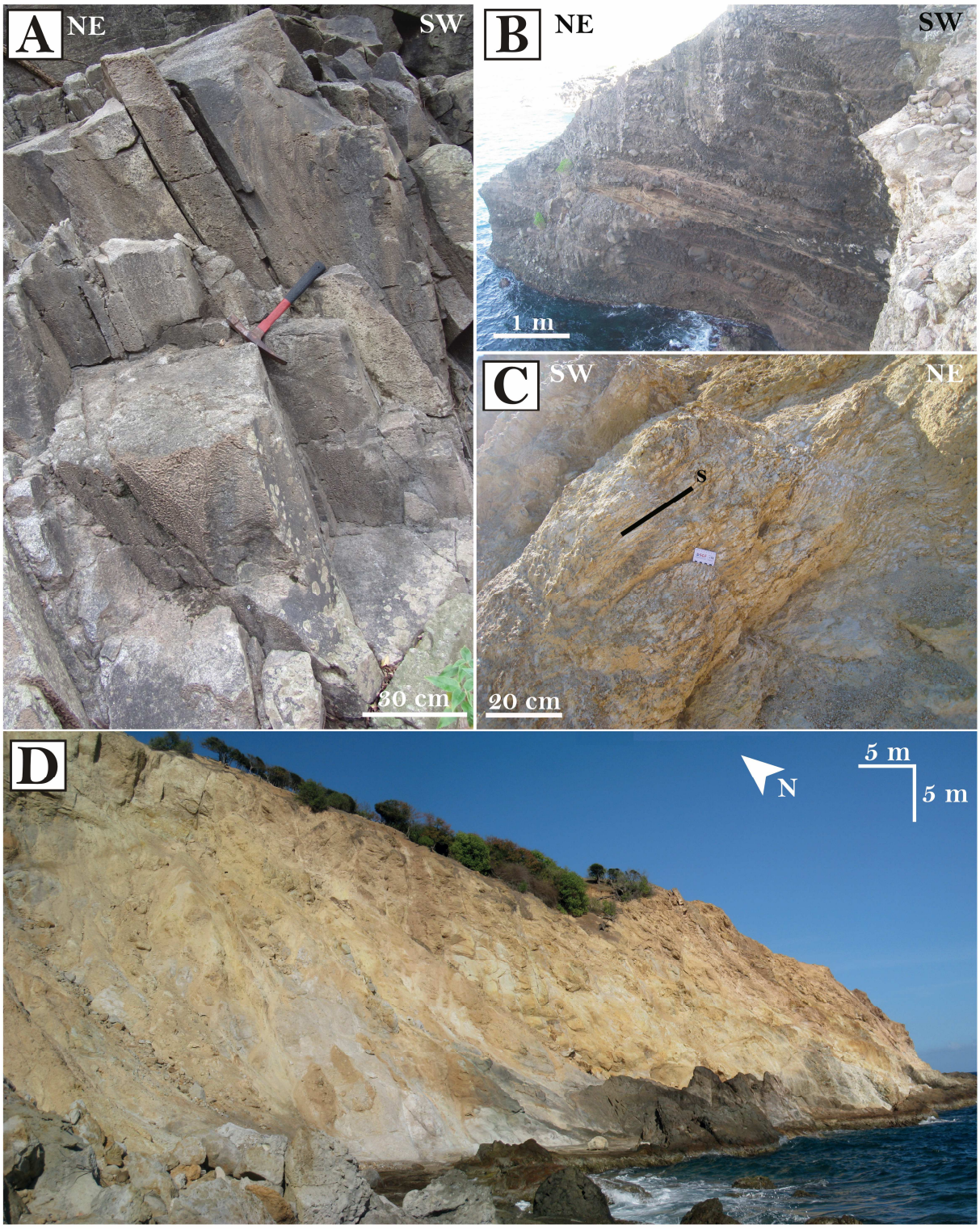

Figure 3: A) Fresh andesitic lava flow from Le Chameau. B) Fresh pyroclastic flow from Pointe Zozio. C) Sampling area (north of Grande Anse beach) in the highly hydrothermalized

area where primary volcanic formations are severely reworked and affected by a schistosity plane (s). D) Sampling area (north of Grande Anse beach) showing intense rock transformations. ***[Color for online version only]***

Figure 4: Selected meta-pyroxene grains (315-500 µm fraction) after magnetic separation, HNO_3 leaching and handpicking. ***[Color for online version only]***

3.1. Electron microprobe analysis

Electron probe microchemical analysis (EPMA), using a CAMECA SX-100 electron microprobe at the "Service Commun de Microsonde" of Montpellier University, was performed on the sample 16STH16 and 16STH19 thin sections to precisely identify the different minerals within the meta-pyroxenes. The operating conditions were a 20 kV accelerating voltage and 10 nA beam current.

3.2. Scanning electron microscopy

Scanning electron microscopy (SEM) and energy-dispersive X-ray spectroscopy (EDX) were performed at the "Centre Commun de Microscopie Appliquée" of the Université Côte d'Azur on the sample 16STH16 and 16STH19 thin sections and polished surfaces using a Tescan Vega 3 XMU SEM system (TESCAN FRANCE, Fuveau, France) equipped with an X-MaxN 50 EDX detector (Oxford Instruments, Abingdon, U.K.) to identify the chemical element distributions and compositions within the meta-pyroxenes. Thin sections were carbon coated, while no coating was used for polished surfaces. Samples were observed and analysed using the low vacuum mode of the SEM (N_2 pressure: 10 Pa for thin sections and 25 Pa for polished surfaces) at an accelerating voltage of 20 kV. EDX results were processed with the Aztec software (version 3.1, Oxford Instruments).

3.3. X-ray diffraction method

3.3.1. Sample preparation

An aliquot of the whitish grains (315-500 µm fraction) was crushed to a fine powder (<70 µm) and was analysed by X-ray diffraction (XRD, Panalytical X'pert Pro system, Bragg Brentano geometry, PIXcel detector $CuK_{\alpha 1+2}$, counting step 0.07° 2θ, angles from 3.5 to 75° 2θ) at the

CEMEF laboratory (Ecole des Mines in Sophia-Antipolis Scientific Centre, France). Mineral identification was established using the Match! software (v. 3.9.0.158, "COD-20190910" database).

Second, in order to characterize microcrystalline phyllosilicates identified in thin sections, we soaked the whitish grains in a $CaCl_2$ solution (250 $g.L^{-1}$) for 4 days to saturate the interlayer spacing of clay minerals with Ca. Later, the mixture of grains and $CaCl_2$ was rinsed with demineralized water up to an electrical conductivity of 40 $\mu S.cm^{-1}$ and centrifuged to recover the dispersed particles in water. The fine particles (<2 µm) were collected for phyllosilicate identification and deposited on a silica glass wafer. XRD analyses were performed on these <2 µm samples (parameters identical to the <70 µm fraction according to angles from 2 to 35° 2θ) at the same CEMEF laboratory. The <2 µm phyllosilicate fractions were analysed under air-drying (AD) with 45% relative humidity and with liquid ethylene glycol (EG) to identify smectites from other minerals (chlorite or illite).

3.3.2. Decomposition of XRD patterns for <2 µm samples

A preliminary decomposition of peaks in AD and EG XRD patterns was performed using the Fityk 1.5 peak fitting software (Wojdyr, **2010**). The different XRD patterns (AD and EG) were decomposed on bands of illite (001), mica (001), chlorite (002), and EG-smectite (001), according to Lanson (**1997**). The full width at half maximum (FWHM) is used to describe the crystallinity or crystal ordering of phyllosilicates with the Kubler (micaceous phases, see below, Kübler, **1967**) and Arkai (chlorite, Árkai, **1991**) indexes. Furthermore, in the remainder of this text, the 10 Å (001) peak with a FWHM lower than 0.17 is described as muscovite, between 0.17 and 0.27 as illite-muscovite, between 0.27 and 0.53 as illite and higher than 0.53 as illite-smectite (Warr & Cox, **2016**). The relative proportions of phyllosilicates were estimated on both the surface and FWHM of decomposed peaks in EG patterns for (001). XRD patterns (AD and EG) of <2 µm samples extracted from the 315-500 µm size fractions were deconvoluted with the PyXRD Linux software developed by Dumon and van Ranst (**2016**). This program compares oriented patterns (AD and EG) and calculated XRD profiles. The calculated XRD allows calculation of the proportion and stacking sequences of muscovite/illite, chlorite, smectite and interlayered illite/smectite.

3.4. Ar-Ar dating

Approximately 500 white grains of meta-pyroxene (Fig. 4) from sample 16STH19 were handpicked under a binocular microscope. Selected grains were packed in aluminium foils for irradiation in the core of the Triga Mark II nuclear reactor at Pavia (Italy) with several aliquots of sanidine from the Taylor Creek Rhyolite standard (28.619 ± 0.034 Ma; Renne *et al.*, **2010**) as the flux monitor. Argon isotope interferences on K and Ca were determined by irradiation of KF and CaF_2 pure salts from which the following correction factors were obtained: $(^{40}Ar/^{39}Ar)_K = 9.69 \times 10^{-3} \pm 3.6 \times 10^{-5}$ at 1σ, $(^{38}Ar/^{39}Ar)_K = 1.297 \times 10^{-2} \pm 4.5 \times 10^{-4}$ at 1σ, $(^{39}Ar/^{37}Ar)_{Ca} = 7.27 \times 10^{-4} \pm 4.0 \times 10^{-5}$ at 1σ, and $(^{36}Ar/^{37}Ar)_{Ca} = 2.88 \times 10^{-4} \pm 1.6 \times 10^{-5}$ at 1σ. The $^{40}Ar/^{39}Ar$ step heating analyses were performed at Geosciences Montpellier (France). After irradiation, four aliquots of bulk sample were analysed (between 100 and 150 grains per analysis). The gas extraction and purification line consisted of (a) an IR-CO2 100 kHz laser used at 3–20% power to heat samples for 180 s, (b) a lens system for beam focusing, (c) a steel chamber, maintained at 10^{-8}–10^{-9} bar, with a copper holder in which 2 mm-diameter blind holes were milled, and (d) two ZrAl getters for purification of gases. Argon isotopes were measured in static mode using an ARGUS VI mass spectrometer. Measurements were carried out in multi-collection mode using Faraday cups. Analyses of atmospheric argon and ^{36}Ar, ^{38}Ar and ^{40}Ar isotopes ('air pipette') were regularly obtained for mass discrimination estimates. The raw data from each step and blanks were processed, and ages were calculated using the ArArCALC software (ArArCalc version 2.52; Koppers, **2002**). Blanks were monitored after every three step heating analyses. All parameters and relative abundance values for each experiment are provided in the supplementary data (Ar/Ar experiments file). The calculated proportions of Ar isotopes were corrected for blanks, mass discrimination, and radioactive decay. Atmospheric ^{40}Ar was estimated using a value of the initial $^{40}Ar/^{36}Ar$ of 298.56 (Lee *et al.*, **2006**). Our criteria for the determination of a plateau

were as follows: a plateau must include at least 60% of released ^{39}Ar over a minimum of three consecutive steps agreeing at the 95% confidence level. Plateau ages are given at the 2σ error level, and the plateau age uncertainties include analytical and J-value errors.
Because through the history of a given geothermal system, several quick spurs of heat from deep below are still possible, the interpretation of age and duration of the studied system will be discussed according to its possible mineralogical evolutions.

4. Results

4.1. Pseudomorphic transformation of volcanic pyroxenes

When comparing all volcanic rocks in the study area, the most spectacular pseudomorphic transformations of pyroxenes are found in hydrothermalized dacites and rhyodacites. Indeed, in the thin sections of these samples, we observe various degrees of pseudomorphic transformation of volcanic pyroxenes in relation to kinetics and thus progress of hydrothermal reactions. In some cases, pyroxenes are only partly replaced by flaky white micas (muscovite, Fig. 5-A). On the other hand, we also observe fully transformed pyroxenes (Fig. 5-B). When the reaction is complete, small patches of flaky particles suggest the occurrence of chlorite and illite or mixed-layered illite/smectite (I-S) minerals (Fig. 5-C). Texturally, fibrous illites or I-S (sheaf felting) are developed at the expense of muscovite. Consequently, in some cases, the product of the fully achieved pseudomorphic pyroxene transformation is a microcrystalline mixture of muscovite+illite (or I-S)+chlorite. In a restricted number of cases, epidote (Fig. 5-D) and titanite are also recognized in flaky particles or thin patches surrounding the pseudomorphosed pyroxenes.

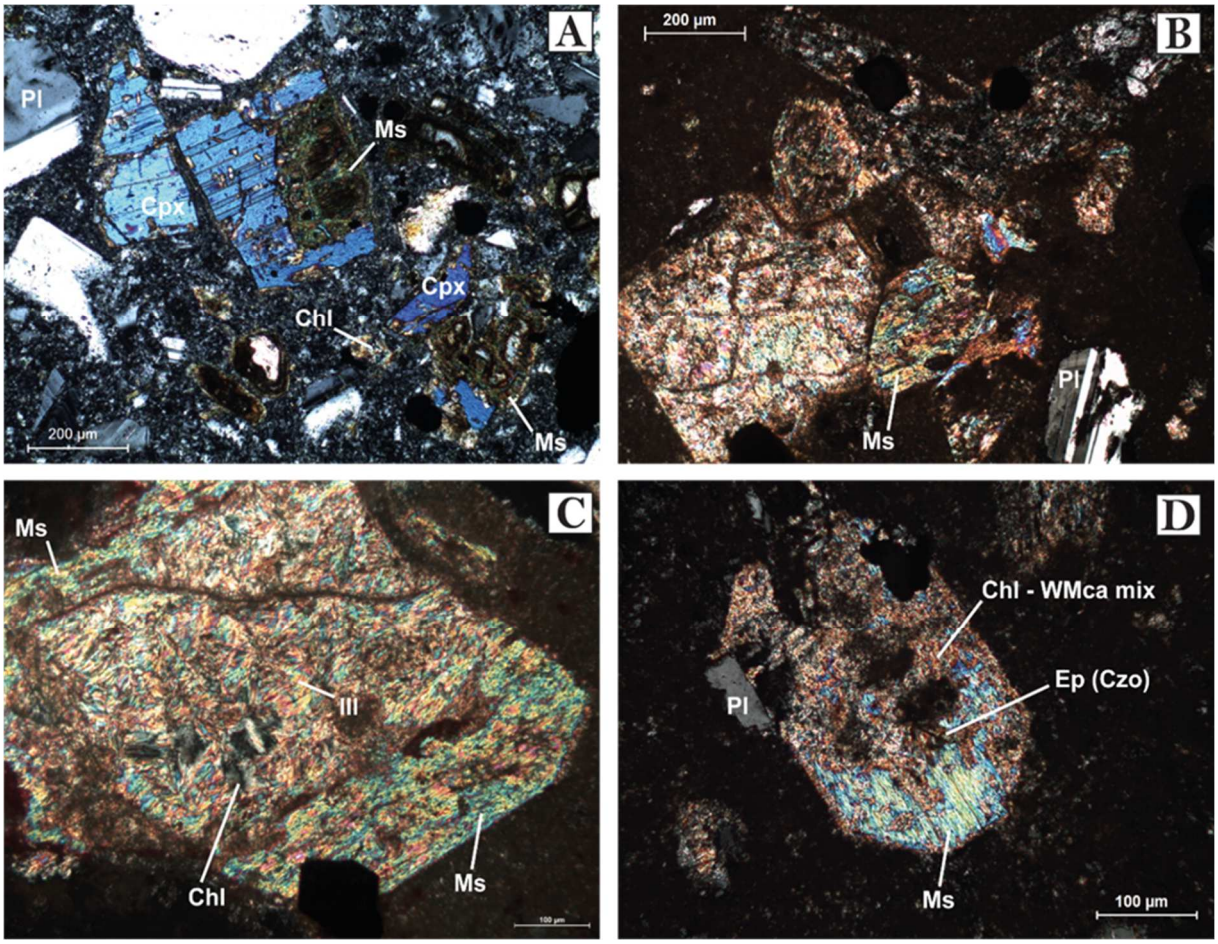

Figure 5: Photomicrographs showing pseudomorphic transformations of pyroxenes A) Thin section of hydrothermalized dacite sample (sample from southwest of Bourg Bay) with partially transformed pyroxene; B) Fully transformed pyroxene in hydrothermalized rhyodacite sample (sample from north of Grande Anse beach, 16STH19); C) Meta-pyroxene with muscovite and chlorite (sample from north of Grande Anse beach, 16STH19); and D)

Meta-pyroxene with fibrous aggregates of chlorite and white micas developed at the expense of muscovite in hydrothermalized dacite sample (sample from north of Grande Anse beach, 16STH16). Chl = chlorite, Cpx = clinopyroxene, Czo = clinozoisite, Ep = epidote, Ill = illite, Ms = muscovite, Pl = plagioclase, Wmca = white mica ***[Color]***

EDX spot analysis and chemical mapping made with SEM on several meta-pyroxenes in thin sections (Fig. 6) and isolated grains allow us to determine their elementary chemical compositions and the average K content (with an average of 5 wt %). Thus, we can identify the K-bearing phases within a wide range of white micas (muscovite +/- illite or I-S) in these grains.

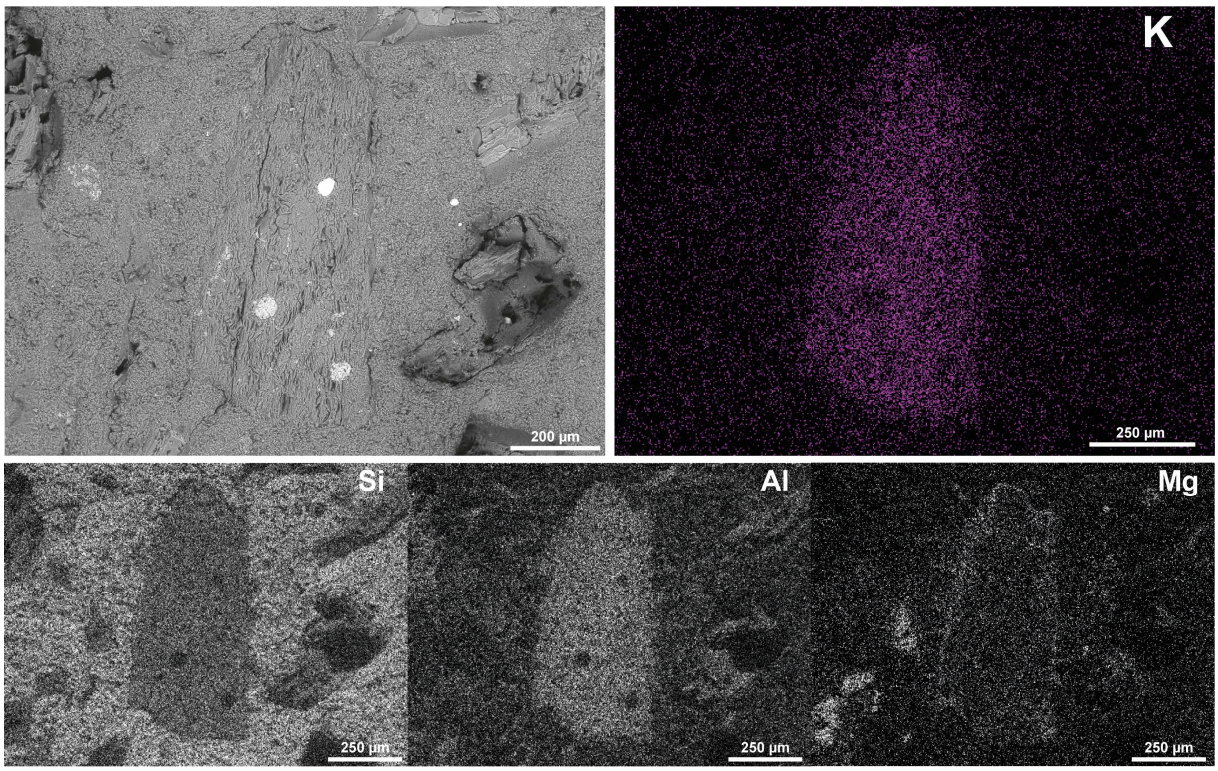

Figure 6: BSE image and chemical compositional maps (K, Si, Al and Mg elements) of muscovite in a meta-pyroxene grain obtained by EDX analyses. ***[Color]***

The large flakes of muscovite, chlorite and the smaller microcrystalline aggregates were analysed with EPMA for major element composition (online supplementary data, Table A.1). The structural formulae of minerals were calculated relative to a structure containing 11 oxygen atoms (muscovite, illite, I-S) or 14 oxygen atoms (chlorite), assuming that the total iron content was composed of Fe^{3+}. In the MR^3-$2R^3$-$3R^2$ diagram (Fig. 7), chlorite and white mica compositions are close to the pure chlorite (sudoite to donbassite types, Wiewióra & Weiss, **1990**) and muscovite end-members, respectively, while the microcrystalline mixtures ranging between muscovite and chlorite compositions are compatible with illite and I-S domains (Fig. 7).

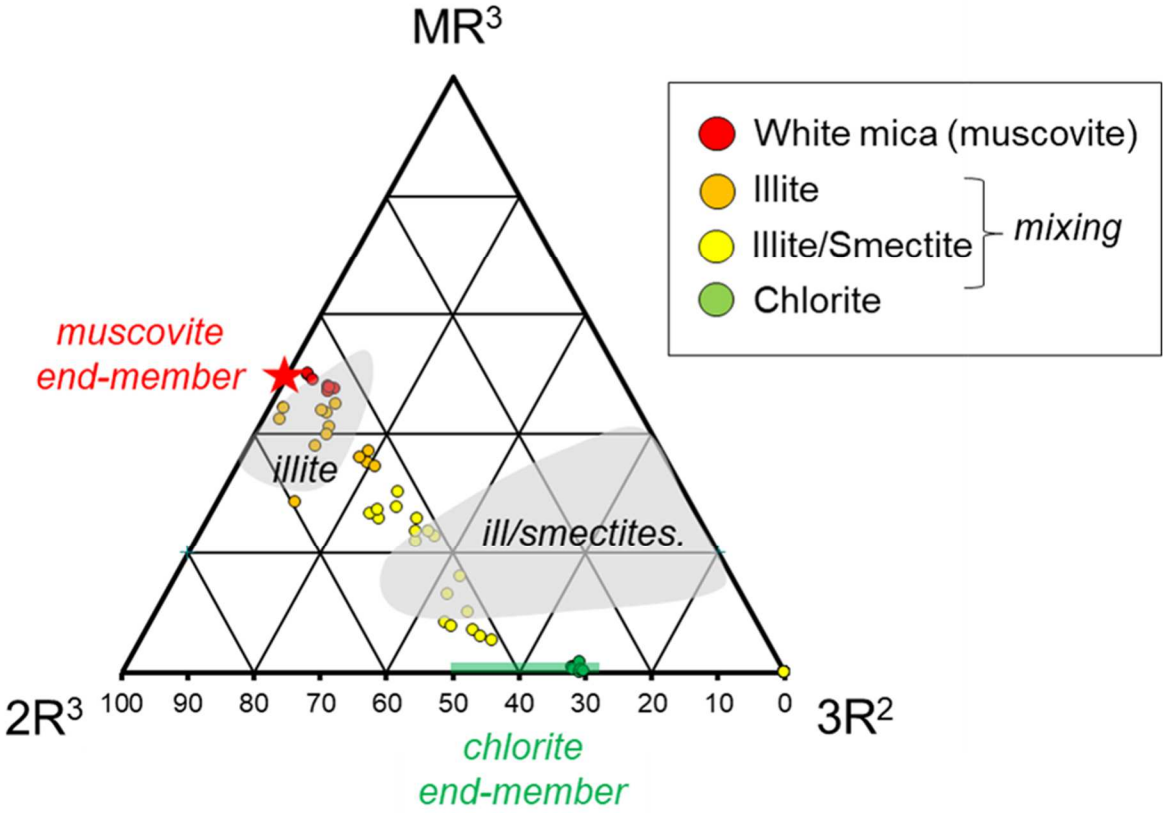

Figure 7: Chemical compositions of secondary phases in the MR^3-$2R^3$-$3R^2$ diagram (Velde, **1985**). Well-distinguished muscovite and chlorite patches, observed in thin sections, are nearly pure end-members. Analyses of undefined microcrystalline aggregates indicate heterogeneous compositions between the illite and illite/smectite fields. Data are available in the online supplementary data (EPMA data – Table A.1). ***[Color]***

4.2. Crystallography and mineralogy of secondary minerals in pseudomorphosed pyroxenes

X-ray diffraction analyses of the separated 315-500 µm fraction hosting the meta-pyroxene grains yield quartz, feldspar, illite-muscovite and chlorite, with no XRD peak for pyroxene (Fig. 8-A). The FWHM of the quartz and feldspar (labradorite) vary from 0.12 to 0.18° 2θ, suggesting that these phases are well crystallized and correspond to volcanic phases. The muscovite-illite and chlorite peaks are expressed at low angles (2 to 20°) and correspond to secondary minerals replacing the primary pyroxenes. The FWHM of (001) mica and chlorite measured on the bulk grain mineralogy with several minerals and the separation of clay-size particles with insufficient material do not allow the identification of mica polytypes (1M, 2M, including 2M1 and 2M2, or 3T type).

To better characterize these mica polytypes, we separated the <2 µm fine particles from the bulk fraction. In this finest fraction, the X-ray patterns (oriented AD and EG, Fig. 8-B) allow us to identify less abundant and small particles roughly recognized in thin sections (Fig. 5-C), i.e., chlorite, smectite, mica, mica-illite and I-S species. The identified relative assemblages for the meta-pyroxenes are reported in Table 1. In order of decreasing abundance (Tab. 1 and online supplementary data in Tab. A.2), we record (Fig. 8-C): (1) pure illite/muscovite with well-crystallized muscovite (small Kübler indexes of 0.12 for (001) mica and 0.53 for (001) illite), (2) pure smectite, (3) interstratified chlorite-smectite (Fig. 8-D), and (4) pure chlorite (with an Arkai index of 0.34). Even in the finest fraction residues of volcanic labradorite can still be observed.

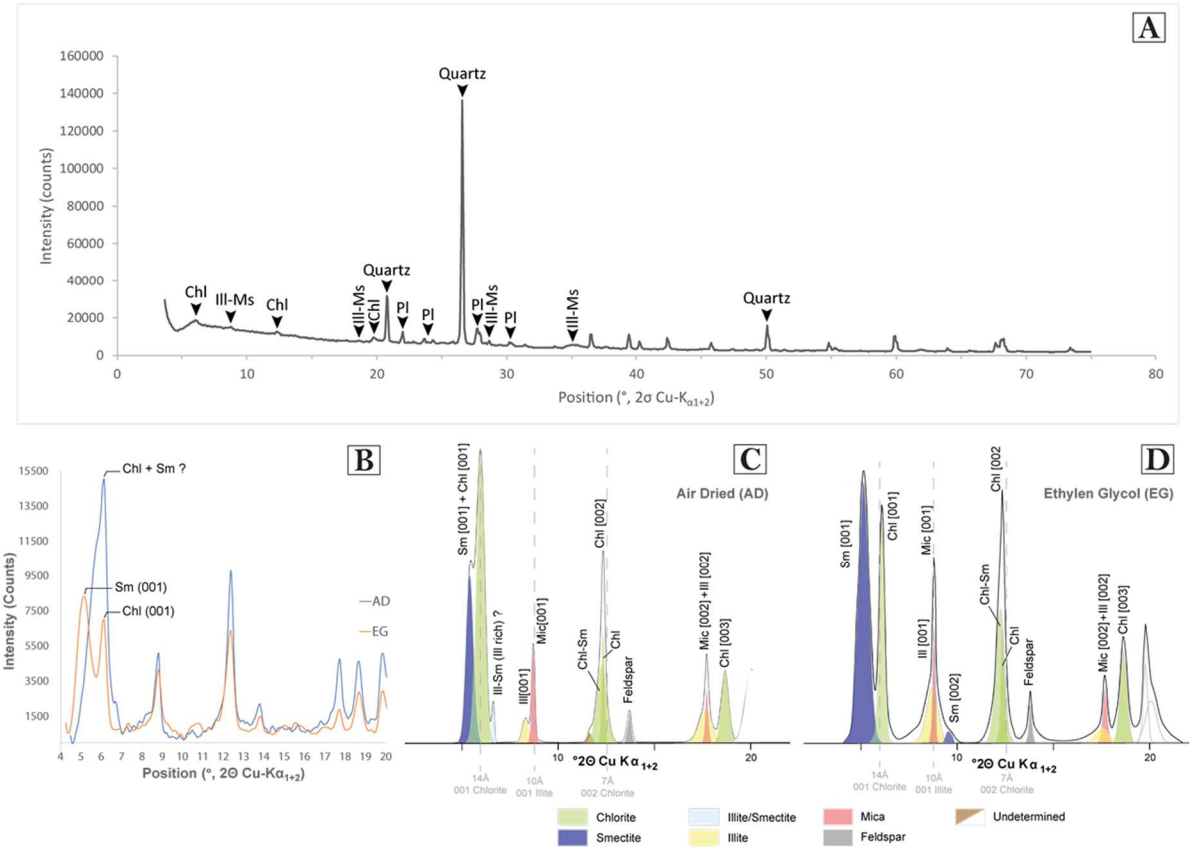

Figure 8: A) XRD bulk meta-pyroxene sample (16STH19); B) Raw X-ray diffraction patterns in AD (air dried) and EG (ethylene glycol) states; C) Decomposed and modelled X-ray patterns in the AD state; D) Decomposed and modelled X-ray patterns in the EG state. ***[Color for online version only]***

Table 1: Results of <2 µm mineral assemblages from the meta-pyroxene using the AD state. The Ãrkaï and Kübler indexes are also reported for detected chlorite, illite and white mica. Estimates of related Tmin values for illite and white mica are determined after Warr and Cox, 2016. Chl = chlorite, Fsp = feldspar, Ill = illite, I-S = interlayered illite-smectite, Musc = muscovite, Sm = smectite. ***[Color for online version only]***

Ãrkai index	Kübler index		Tmin values [001 illite]	Tmin values [001 mica]	<2µm assemblage
002 chlorite	001 illite	001 mica	(Warr and Cox, 2016)	(Warr and Cox, 2016)	
0.34	0.53	0.12	>200°C	>350°C	Ill-Musc, Sm, Chl-Sm, Chl, Fsp

The K-rich phases, which can play a role in the obtained $^{40}Ar/^{39}Ar$ dataset, are well identified in our sample: muscovite, illite and interstratified I-S. Other phases without potassium (chlorite, smectite, quartz, labradorite, epidote, titanite or absent pyroxene) can be neglected compared to K-bearing phases.

4.3. Ar-Ar results

All detailed data for each experiment are provided in the online supplementary data (Ar/Ar experiments file) with a compilation of Ar-Ar results available in Table A.3.

As previously mentioned, four aliquots of the same sample (16STH19B) were replicated. The first experiment (16STH19B B7-B8) yields a well-defined plateau age of 2.78 ± 0.23 Ma, corresponding to 97.6% of ^{39}Ar released (Fig. 9-A). The inverse isochron calculation yields an identical age of 2.77 ± 0.33 Ma with an initial $^{40}Ar/^{36}Ar$ ratio of 299.9 ± 12.6, indicating that the trapped $^{40}Ar/^{36}Ar$ is indistinguishable from atmospheric $^{40}Ar/^{36}Ar$. The second and third experiments (16STH19 A9-A10 and 16STH19 B12) display concordant plateau ages at 2.45 ± 0.25 Ma and 2.62 ± 0.20 Ma, with 87.3% and 98.9% of ^{39}Ar released, respectively (Fig. 9-

B-D). Inverse isochron ages and related initial $^{40}Ar/^{36}Ar$ ratios for these two experiments are concordant with those for the first aliquot. The fourth experiment, 16STH19B B2, yields a less well-defined plateau age of 2.55 ± 0.44 Ma (Fig. 9-C), with 61% of ^{39}Ar released due to higher ^{40}Ar atmospheric contamination. Nevertheless, all plateau ages are concordant; thus, we can statistically combine these four experiments. We retain the combined plateau age at 2.59 ± 0.12 Ma at 2σ (MSWD 0.39) for meta-pyroxenes (Fig. 9-E). K/Ca spectra (deduced from $^{39}Ar_K/^{37}Ar_{Ca}$ spectra) associated with the four plateau ages display relatively regular flat patterns, highlighting the chemical reproducibility of the step-heated phase(s).

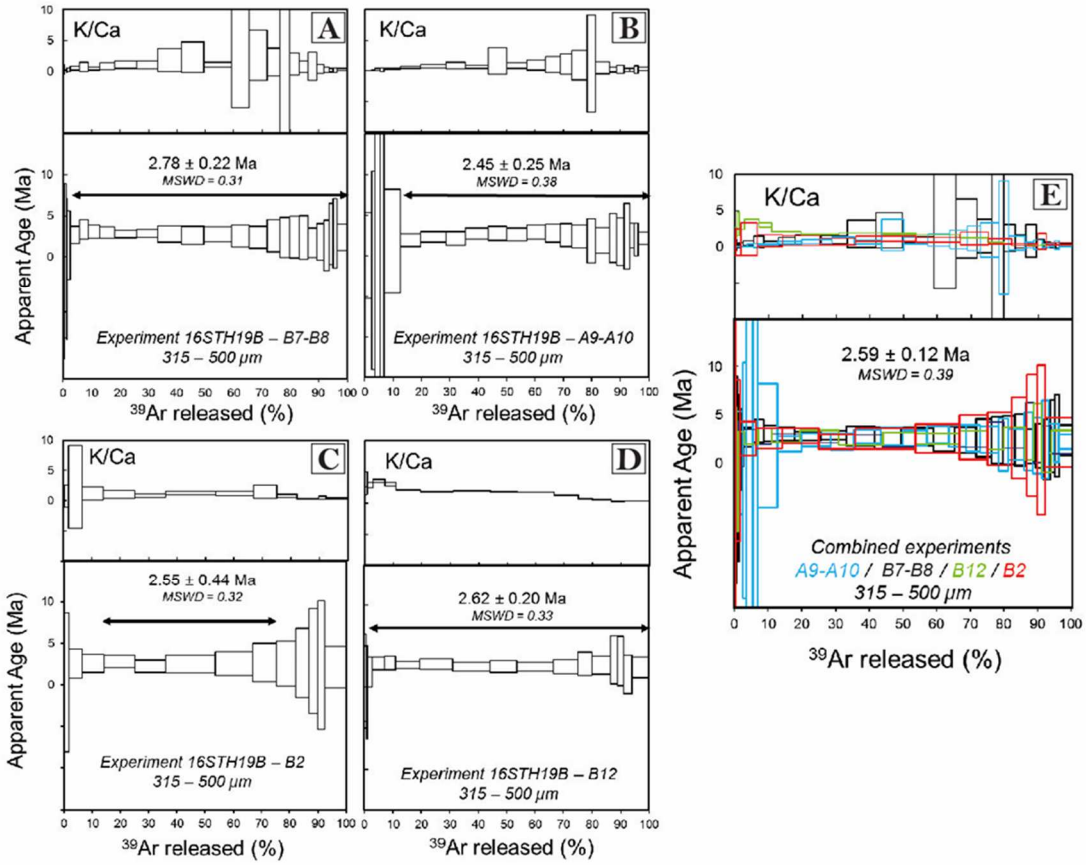

Figure 9: $^{40}Ar/^{39}Ar$ age spectra and K/Ca spectra as functions of ^{39}Ar released. The error boxes of each step are at the 2σ level. Arrows show the plateau age fraction. The error of the plateau age is given at the 2σ level. A, B, C and D: Four individual experiments on the meta-pyroxene 315-500 µm fraction; E: Combined spectra of the four experiments A+B+C+D. ***[Color]***

5. Discussion

Based on previously described petrographic and mineralogical observations, the evolution observed in meta-dacites or meta-rhyodacites resulted mainly in the development of white micas and chlorite at the expense of pyroxenes during the high temperature stage. Microcrystalline clay mineral assemblages developed afterward during the low-temperature stage of the hydrothermal system. This process requires (1) significant H_2O-rich fluid infiltration through the pore space of the rocks and the volcanic groundmass with partial dissolution of at least anorthoclase microlites, which are the only possible local source of K, and (2) transfer of K, Si, and Al in the fluid-free phase until contact with pyroxene phenocrysts.

5.1. Influence of K-rich phase crystallinity on Ar-Ar result interpretations

Interstratified I-S species with low crystallinity are frequently developed at the expense of muscovite in numerous hydrothermal systems (Inoue *et al.*, **1992**; Inoue & Kitagawa, **1994**).

This mineralogical transformation would perturb the previous K-bearing phase chronometer and thus would provide complex and disturbed Ar-Ar spectra. Nevertheless, we obtain well-defined Ar-Ar plateau ages from the analysed meta-pyroxene grains, which is most likely due to the abundance of muscovite with high crystallinity in the pseudomorphic assemblage. However, the analysed grains are a mixture of mainly muscovite and various proportions of clay minerals, including K-rich phases, i.e., illite and I-S that crystallized at different temperatures and thus at different times. The flat K/Ca spectrum that we obtained in all replicates does not resemble that of biphasic assemblages. This result suggests that cooling was fast enough to preserve muscovite from low-temperature transformations. Because of the presence of illite, we could not exclude a possible ^{39}Ar recoil effect and thus disturbed ages, as previously described by various authors (Dong *et al.*, **1995**; Hall *et al.*, **1997**; Isik *et al.*, **2014**). Indeed, the recoil effect, occurring during neutron irradiation, affects < 50 µm microcrystals (Jourdan *et al.*, **2007**) and here specifically the illite species. However, the reproducibility of our four individual experiments (Fig. 9), without typical recoil spectra, enhances the reliability of the Ar-Ar plateau age obtained.

5.2. Influence of hydrothermal system cooling on Ar-Ar results

In thin sections, we observe the development of illite at the expense of well-crystallized muscovite grains (Fig. 5-C). This observation is consistent with other studies indicating that under low-grade metamorphism as well as under hydrothermal alteration conditions, the secondary micas developed at the expense of pyroxenes are often mixed illite and muscovite (Meyer & Hemley, **1967**; Merriman & Peacor, **1998**). Moreover, several studies have demonstrated that muscovite develops in epithermal to mesothermal systems at temperatures above 300°C (Guilbert & Park, **1986**; White & Hedenquist, **1990**; Groves *et al.*, **1998**; Hedenquist *et al.*, **2000**; Goldfarb *et al.*, **2001**), while illite is stable at lower temperatures, and its crystallization is generally the result of cooling of the hydrothermal system (~150°C, Henley & Ellis, **1983**; Hedenquist *et al.*, **2000**; Ji & Browne, **2000**; Warr & Cox, **2016**). It therefore seems important to test the effect of illite development during cooling of the studied samples on our Ar-Ar results.

To quantify the effect of illite development on the muscovite age, we propose a theoretical model showing how progressive illite formation modifies the K-Ar systematics of muscovite and ultimately can affect the accuracy of muscovite ages.

The calculations proposed for sericitization of plagioclases by Verati and Jourdan (2014) are hereafter similarly applied to muscovite and illite in pseudomorphosed pyroxenes. This calculation evaluates the K-Ar age reductions of illitized muscovite with a two-component mixture between hydrothermal primary muscovite and secondary illite, considering that illitization occurs in a single stage.

Using the K-Ar age equation, for a given K content in muscovite ($^{40}K_{ms}$), the radiogenic ^{40}Ar in illite-free muscovite with an age t is:

$$^{40}Ar = \frac{\lambda_e}{\lambda} {}^{40}K_{ms}(e^{\lambda t} - 1)$$

For muscovite that is illitized at t' (t'<t), with X% illite in the mixture, for a given K content in illite ($^{40}K_{ill}$), the total amount of K content in the mixture ($^{40}K_{tot}$), as well as the total amount of radiogenic ^{40}Ar ($^{40}Ar_{tot}$) in the mixture, are:

$^{40}K_{tot} = (1 - X)^{40}K_{ms} + X^{40}K_{ill}$ with $^{40}Ar_{tot} = {}^{40}Ar_{ms} + {}^{40}Ar_{ill}$

We obtain:

$$^{40}Ar_{tot} = \frac{\lambda_e}{\lambda} {}^{40}K_{ms}(e^{\lambda t} - 1) + \frac{\lambda_e}{\lambda} {}^{40}K_{ill}(e^{\lambda t'} - 1)$$

We can define the apparent age t'' of the two-component mixture (illitized muscovite) as follows:

$$^{40}Ar_{tot} = \frac{\lambda_e}{\lambda} {}^{40}K_{tot}(e^{\lambda t''} - 1)$$

The previous equations may be combined to give:

449 $$\frac{\lambda_e}{\lambda}{}^{40}K_{tot}(e^{\lambda t''}-1)=\frac{\lambda_e}{\lambda}{}^{40}K_{ms}(e^{\lambda t}-1)+\frac{\lambda_e}{\lambda}{}^{40}K_{ill}(e^{\lambda t'}-1)$$

450 We deduce the apparent K-Ar age t'' of the mixing:

451 $$t'' = \frac{1}{\lambda} ln\left[1+\left(\frac{^{40}K_{ms}}{^{40}K_{tot}}\right)(e^{\lambda t}-1)+\left(\frac{^{40}K_{ill}}{^{40}K_{tot}}\right)(e^{\lambda t'}-1)\right] \quad (\textbf{\textit{VI-1}})$$

452

453 where $^{40}K_{ms}$ is the ^{40}K content of muscovite, $^{40}K_{ill}$ is the ^{40}K content of illite, $^{40}K^{tot}$ is the ^{40}K
454 content of the mixture, t is the K-Ar hydrothermal age of the muscovite, t' is the K-Ar age of
455 the illitization event and λ is the total ^{40}K decay constant (here 5.544 x 10^{-10} yr^{-1} after Steiger
456 & Jäger, **1977**).
457 The % of K-Ar age reduction AR is defined as:

458 $$AR = \frac{t-t''}{t} \quad (\textbf{\textit{VI-2}})$$

459

460 The $^{40}K_{ms}/^{40}K_{tot}$ and $^{40}K_{ill}/^{40}K_{tot}$ ratios in equation (***VI-1***) are calculated with M_{ms} = 398.71
461 $g.mol^{-1}$, M_{ill} = 389.34 $g.mol^{-1}$, weight % of K_2O_{ms} = 11.81%, and that of K_2O_{ill} = 7.26%. The t
462 value in equation (***VI-2***) is the K-Ar age of the muscovite, i.e., the total fusion age of the
463 combined Ar-Ar experiments (2.45 ± 0.27 Ma, see Table A.3 in the online supplementary
464 data).
465 According to the modelling of Verati and Jourdan (**2014**), the variable parameters in our
466 study are the age of the illite (t') and the amount of illitization. In Figure 10, we plot eight
467 curves (different time spans between muscovite crystallization and illitization) showing the
468 %AR versus the % of illitization. The age difference between muscovite crystallization and
469 illitization is the main parameter influencing the calculated K-Ar age reduction (Fig. 10).
470 Regardless of the amount of illitization (the 2σ error of the K-Ar age is larger than the time
471 span), if the time span between illitization and muscovite ranges between 0 and 10%, the
472 decrease in the K-Ar age is not significant enough to provide a mixing K-Ar age discordant
473 from the muscovite age. This result implies a fast cooling rate (>150°C/200 ka) for the
474 Saintes hydrothermal system.
475

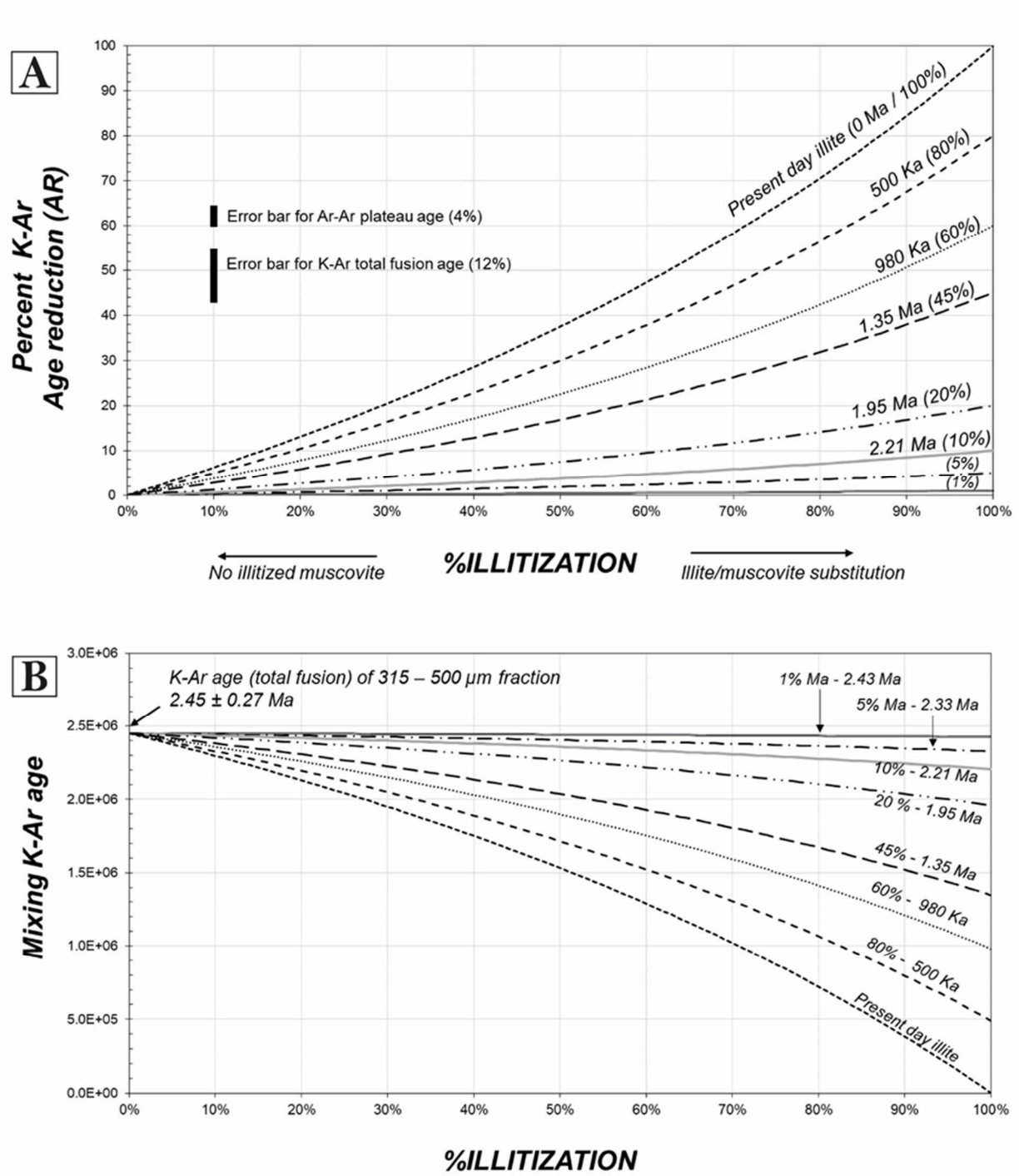

Figure 10: A) Age reduction parameter (%AR) vs. % muscovite illitization. The curves are calculated for different t' (age of illitization). The muscovite age t = the K-Ar total fusion age of 2.45 ± 0.27 Ma (see text for explanation). The age of the illitization (% time span/muscovite) is specified for each curve. Error bars for K-Ar total fusion and Ar-Ar plateau age are reported (after error at 2σ in Table A.3 in online supplementary data). B) Theorical mixing K-Ar age vs. % muscovite illitization. K-Ar age of 2.45 ± 0.27 Ma for the 315-500 µm fraction is reported. Different theoretical curves are defined according to different ages for illitization (2.43 Ma to present day). For example, muscovite at 2.45 Ma displays an apparent K-Ar of 2.0 Ma with 50% illitization occurring at 1.35 Ma. ***[Black and White]***

For a difference in age of 20% to 100% between muscovite crystallization and illitization, the related %AR remains low (<40%) for a high percent of alteration of 50%. High amounts of

illitization (70 – 90%) do not totally reset the muscovite age regardless of the time span between crystallization and illitization.

5.3. Les Saintes cooling rate in the tectonic framework of the Lesser Antilles arc

The intra-oceanic subduction of the North-American plate beneath the Caribbean plate drives the Lesser Antilles magmatic arc (Martin-Kaye, 1969; Bouysse and Westerkamp, 1990) and the oblique convergence between these two plates is accommodated by crustal-scale strain partitioning and development of trench parallel extension (Feuillet et al., 2001, 2002). In this context the Guadeloupe archipelago is affected by a transtensive regime with development of both normal and strike-slip faults (Feuillet et al., 2002; Calcagno et al., 2012; Mathieu et al., 2013). Such a framework is favourable for significant and fast vertical movements in the arc crust (see discussions in Feuillet et al., 2004; Münch et al., 2013; Leclerc et al., 2016; Verati et al., 2018). The fast cooling rate obtained for Les Saintes hydrothermal system is consistent with this tectonic pattern and emphasizes also rapid exhumation of some pieces of the shallow arc crust under significant extension and erosion rates.

5.4. Implications for the duration of geothermal systems in magmatic arcs

The combined plateau age at 2.59 ± 0.12 Ma at 2σ is the best age estimate of the high temperature hydrothermal system (>300°C) recognized on Terre-de-Haut Island. This age was obtained on a volcanic island for which other temporal constraints are available. We thus have the opportunity to test the robustness of our chronological results by a comparison with the ages obtained for volcanic activity on this island (emplacement of lava flows, volcanic domes or plugs, Fig. 1-B). Indeed, as highlighted in Fig.1-C hydrothermal transformations are gradually developed according to the finite deformation gradient observed in the field. As a consequence of this heterogeneous strain pattern, various volcanic formations are progressively affected by the high-temperature hydrothermal transformations, and thus when we date a volcanic flow outside of a given hydrothermalised shear zone, we date the protolith of the altered formation and we obtained a “oldest” limit for the geothermal activity. Of course, because we cannot identify all the volcanic protoliths involved in the highly altered zone, we cannot definitely discard the possibility of an activity of the geothermal system before the oldest dated volcanic formation. A first dataset was obtained (Jacques *et al.*, **1984**) by the K/Ar technique on whole-rock samples but did not consider the impacts of hydrothermal and/or supergene alteration processes on the ages. However, the results obtained with this approach, in the whole Lesser Antilles arc, are now considered outdated because of significant K loss and Ar enrichment potentially associated with alteration (see discussion in Samper *et al.*, **2007**, **2009**). A more recent dataset of K-Ar ages (Zami *et al.*, **2014**) was obtained by the unspiked K-Ar technique using measurements on the groundmass only from a selection of fresh rocks, as proposed by Samper *et al.* (**2007**, **2009**). Thus, the volcanic activity of Terre de Haut Island has been bracketed between 2.98 ± 0.04 Ma and 2.00 ± 0.03 Ma. Within this framework, the hydrothermal study area is intruded by several volcanic plugs and domes (Fig. 1-B). In addition, these intrusive volcanic plugs and domes are totally unaltered and are thus not affected by hydrothermal alteration. Among these unaltered volcanic intrusives, the “Chameau” volcanic dome is dated at 2.00 ± 0.03 Ma (Fig. 1-B, Zami *et al.*, **2014**). This age represents the uppermost or youngest limit for the activity of the hydrothermal system.

However using this result in order to approach the duration of the studied geothermal system implies to assume that the heat flow has remained stable through the geothermal history of Guadeloupe archipelago. The present-day conductive geothermal gradient was measured around the Guadeloupe archipelago in the range 69.3 ± 1.5 and 98.2 ± 8.8 °C/km (Manga et al., 2012). As demonstrated by recent mineralogical, petrological and geochronological investigations on the oldest hydrothermal metamorphic meta-volcanites recognized in this archipelago, this conductive gradient did not change during the last 5 Ma (Verati et al., 2018; Favier et al., 2019; Favier et al., 2021). We can therefore reasonably consider a stable heat flow over this time span. This assumption is consistent with the fact that the regional stress field also has remained unchanged since 5 Ma in the Guadeloupe archipelago (Feuillet et al.,

2002, 2004; Mathieu et al., 2011; Corsini et al., 2011; Lardeaux et al., 2013; Münch et al., 2013; Leclerc et al., 2016). However, during the operation of a given geothermal system, quick spurs of heat from deep below can always be considered. In a companion paper (Favier et al, 2021), we modelled the P-T stability fields of all the expected mineral assemblages for the studied chemical system. Under constant pressure, at 400°C, titanite is replaced by rutile, and epidote is replaced by zoïsite, while and at around 480°C, muscovite disappears and biotite, cordierite and rutile are diagnostic phases. We never observed such mineral reactions in Terre-de-Haut hydrothermal zone. We can therefore discard the hypothesis of quick heat pulses leading development of higher thermal conditions. Of course, if such pulses lead development of constant temperature conditions, similar mineral assemblages are expected to crystallize and it will be impossible, by mineral and petrologic investigations, to distinguish these incremental heat inputs in a steady-state stable thermal gradient.

Taking into account all the assumptions presented and discussed in previous paragraphs, our new results are clearly consistent with the age database obtained by Zami *et al.* (**2014**), and the following points must be emphasized:

- First, the development of the studied hydrothermal system, regarded as an analogue of a high temperature geothermal system, was coeval with the volcanic activity on this island.
- Second, overall, the whole temporal dataset allows us to estimate a maximal duration of 650 ka (i.e., the time difference between the hydrothermal event dated at 2.59 ± 0.12 Ma, and the intrusion of the unaltered “Chameau” volcanic dome dated at 2.00 ± 0.03 Ma) for the Saintes hydrothermal system.

To test the robustness of this result, it is quite interesting to compare it to the age well-know active geothermal system of Bouillante Bay (west coast of Guadeloupe, Bouchot et al., 2010; Thinon et al., 2010). The $^{40}Ar/^{39}Ar$ dating of this high-enthalpy geothermal system, based on an adularia bearing hydrothermal breccia, indicates that the geothermal activity archipelago, still active, started at least 248.2+50.2 ka ago (Verati et al., 2014). Moreover, the estimated duration of the studied hydrothermal system is in agreement with the few available lifetimes obtained for other volcanic geothermal provinces or epithermal deposits located worldwide where hydrothermal activity ranges between a few hundred thousand years and a million years (Faure, **1986**; Deloule & Turcotte, **1989**; Nakai *et al.*, **1993**; Barnes, **1997**; Rowland & Sibson, **2004**; Grimes et al., 1998 ; Velador et al., 2010). Last the proposed operating duration for the Saintes hydrothermal system, is also in agreement with thermal modelling of convective hydrothermal systems around shallow magmatic intrusions completed within tens of thousands of years to almost 1 Ma (Carslaw and Jaeger, 1959; Jaeger, 1959, 1968; Delaney, 1982; Kissling, 1999; Eldursi et al., 2009; Carrrichi et al., 2012; Hoinkes et al., 2005).

This dating approach could also be carried out on younger geothermal systems (< 300 ka) that are of particular interest for geothermal exploration in active volcanic systems. The most important constraint on obtaining ages with the stepwise heating technique or total fusion analyses on multigrain separates is to evaluate the minimal masses of required material to detect enough radiogenic ^{40}Ar in the samples. Dating such young geothermal materials is challenging because of the high content of atmospheric ^{40}Ar compared to radiogenic ^{40}Ar. In particular, we observe that Les Saintes metapyroxenes display a high atmospheric contamination with a mean value at 60%. Unfortunately, for young samples, error magnification begins to dominate when the proportion of radiogenic ^{40}Ar is less than about 10% of the total ^{40}Ar and increase exponentially (McDougall and Harrison, 1999). In such case, taking into account (1) the K-content of metapyroxenes, (2) the atmospheric ^{40}Ar contribution of such hydrothermal minerals and (3) the detection limits of the most recent multicollector mass spectrometers, we estimate for a 300 ka old sample that a minimum of 10 mg and 100 mg are required for total fusion on multigrain aliquots and stepwise heating analyses respectively (Fig. A-1).

6. Conclusions

1. We confirm that, even for complex reaction microstructures, the $^{40}Ar/^{39}Ar$ method, coupled with a high-resolution mineralogical analysis, is a powerful technique for dating high temperature hydro/geothermal systems. Under temperatures ranging from 400-200°C, the degree of crystallinity of K-bearing phases is a key parameter for accurate Ar-Ar dating, especially for muscovite.
2. Muscovites from hydrothermally altered pyroxenes with high crystallinity indexes and less than 40% illitization can provide accurate Ar-Ar plateau ages of crystallization for temperatures above 300°C. Illitization can have a fundamental impact on the Ar-Ar and K-Ar systematics only if the muscovite is highly illitized and/or if the illitization is much younger than the muscovite crystallization.
3. We report the first example of dating hydrothermal muscovite crystallization developed at the expense of meta-pyroxenes within transformed arc-related calc-alkaline volcanic rocks. This approach allows us to propose an age of 2.59 ± 0.12 Ma for the development of the Terre-de-Haut fossil geothermal reservoir, with a maximal lifetime estimated at 650 ka.
4. Our modelling implies a fast cooling rate (>150°C/200 ka) for the Saintes hydrothermal system. This cooling rate has significant consequences for the stability and preservation of high temperature hydrothermal mineral phases over time. This first cooling rate estimate deserves to be challenged by dating other K-bearing hydrothermal minerals developed under lower temperature hydrothermal activity, such as jarosite, which is potentially present in the area of interest.

7. Acknowledgments

This paper is a contribution to the GEOTREF program, funded by the French government with the “Investissements d’Avenir” program and tutored by ADEME. We thank the researchers from the GEOTREF consortium for greatful discussions during the fieldwork campaigns in Guadeloupe and during scientific meetings. The authors thank Arthur Iemmolo for his technical support during $^{40}Ar/^{39}Ar$ analysis, Magali Bonnefoy and Matthieu Zanti for sampling preparation, Gabriel Monge for his welcome to CEMEF for the use of the X-ray Diffraction device, Emile Voitus for his participation in the fieldwork campaigns and to the residents of the Terre-de-Haut Island. CCMA electron microscopy equipments have been funded by the Région Sud - Provence-Alpes-Côte d'Azur, the Conseil Départemental des Alpes Maritimes, and the GIS-IBiSA. Finally, we are grateful to Pr. Balz Kamber for editoral work and to two anonymous reviewers for their useful thoughts and constructive reviews which improved the manuscript.

8. Appendices

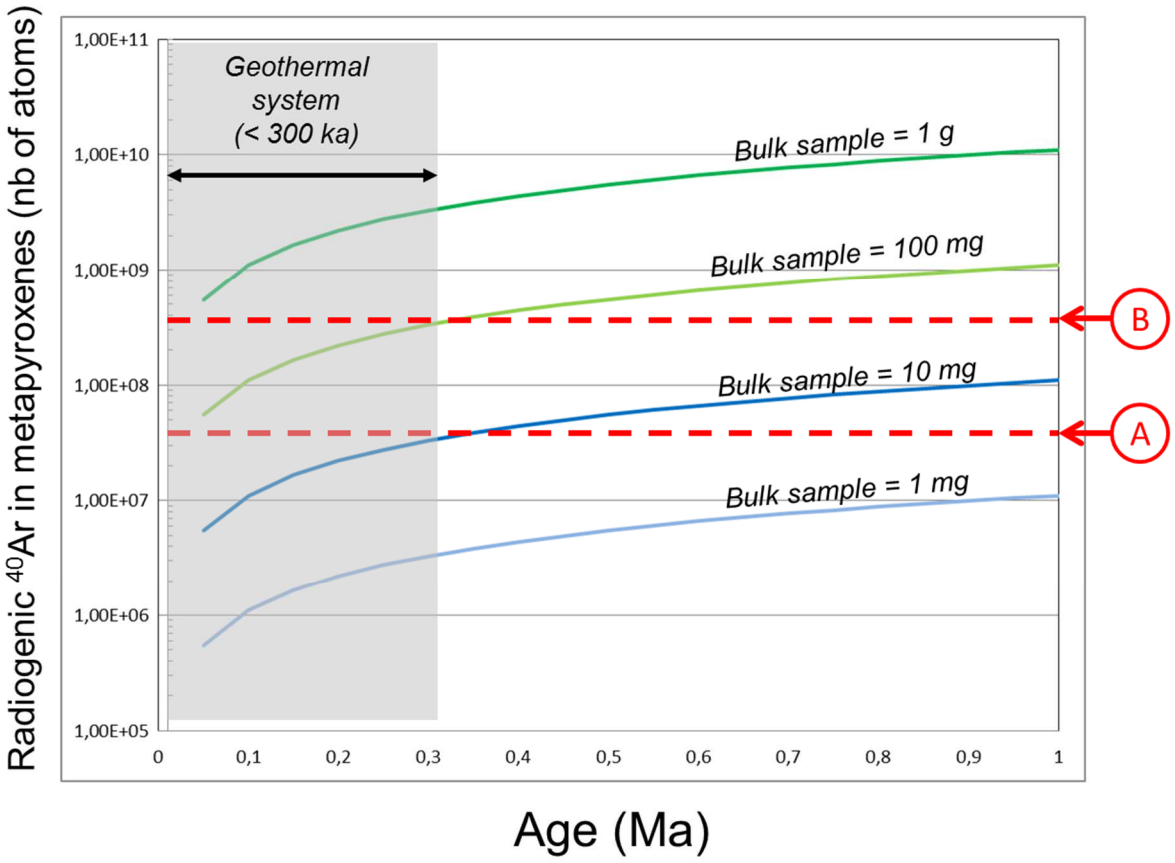

Figure A.1 - Blue and green curves correspond to the amount of cumulated radiogenic ^{40}Ar with time (< 1 Ma) in 1 mg, 10 mg, 100 mg and 1g of metapyroxene bulk sample respectively (K_2O = 11.82 wt%; $^{40}K/K_{tot}$ = 0,0001167; λ = 5.544E^{-10} yr^{-1}; $\lambda\varepsilon$ = 5.81E^{-11} yr^{-1}; N_A = 6.022 × 10^{23} mol^{-1}).
Red lines represent the analytical detection limits for mass spectrometer (ARGUS VI), i.e lines below which ^{40}Ar can no longer be detected against the background signal. Line A is related to total fusion experiment on multigrain aliquots, which must be repeated at least 10 times to obtain an inverse isochron. Line B is related to stepwise heating technique on a single aliquot (10 steps) which provides Ar-Ar spectra. Calculations were made according to: (1) measurements were carried out in multi-collection mode using Faraday cups equipped with 10^{12} ohm, (2) the acquisition time for each step is 600 seconds, (3) sensitivity was estimated knowing that a signal of 1 fA (10^{-15} A) corresponds to a rate of 6000 ions per seconds, (3) the measured ^{40}Ar peak must be five times higher than the monitored blanks.
For example, we can estimate for a 300 ka old sample that a minimum of 10 mg and 100 mg are required for total fusion on multigrain aliquots and stepwise heating analyses respectively. For a 200 ka old sample 100 mg are required for total fusion technique, and 1 g for step heating technique.

Table A.1 – Electron microprobe analyses and structural formula of high-temperature hydrothermal phases ***[Supplemental file: Excel file version]***

Mineral	Illite-Smectite															
analysis number	1 / 1 .	3 / 1 .	4 / 1 .	5 / 1 .	9 / 1 .	10 / 1 .	14 / 1 .	27 / 1 .	15 / 1 .	31 / 1 .	32 / 1 .	35 / 1 .	37 / 1 .	45 / 1 .	46 / 1 .	41 / 1 .
Element (%wt oxide)																
Al2O3	29.94	27.44	24.62	26.14	28.18	26.20	26.10	29.84	27.03	27.48	28.15	29.55	24.73	24.48	23.31	29.26
SiO2	45.55	41.51	36.88	41.59	43.51	43.05	40.07	43.79	41.66	39.69	41.78	42.79	40.01	39.45	39.11	42.76
TiO2	0.09	0.08	0.07	0.09	0.06	0.06	0.09	0.04	0.09	0.03	0.03	0.02	0.02	0.14	0.16	0.03
Na2O	0.08	0.05	0.03	0.03	0.07	0.03	0.03	0.10	0.04	0.06	0.11	0.09	0.03	0.02	0.03	0.09
MgO	9.42	11.88	19.28	14.57	9.57	8.53	14.04	10.24	12.18	16.50	10.59	7.92	19.18	15.24	13.65	10.57
MnO	0.82	0.76	1.28	0.98	0.65	0.55	1.08	0.65	0.97	0.90	0.64	0.48	0.90	1.12	1.23	0.52
FeO	0.94	1.70	2.81	1.96	1.34	1.33	1.77	1.21	1.53	1.69	1.34	0.98	1.96	2.04	1.79	1.21
K2O	6.51	5.19	2.20	3.33	6.00	6.64	3.68	3.93	4.58	3.70	3.46	6.04	1.17	3.85	3.99	3.79
CaO	0.21	0.26	0.37	0.38	0.30	0.25	0.31	0.34	0.28	0.31	0.45	0.26	0.66	0.30	0.38	0.53
Total	93.56	88.88	87.53	89.07	89.68	86.64	87.18	90.14	88.35	90.36	86.54	88.12	88.64	86.65	83.65	88.76
Structural formula																
Al	**2.36**	**2.29**	**2.11**	**2.17**	**2.33**	**2.24**	**2.22**	**2.41**	**2.26**	**2.26**	**2.37**	**2.47**	**2.05**	**2.11**	**2.08**	**2.41**
Si	**3.05**	**2.94**	**2.68**	**2.93**	**3.05**	**3.13**	**2.89**	**3.01**	**2.96**	**2.77**	**2.99**	**3.03**	**2.82**	**2.88**	**2.96**	**2.98**
Ti	**0.00**	**0.00**	**0.00**	**0.01**	**0.00**	**0.00**	**0.01**	**0.00**	**0.00**	**0.00**	**0.00**	**0.00**	**0.00**	**0.01**	**0.01**	**0.00**
Na	**0.01**	**0.01**	**0.00**	**0.00**	**0.01**	**0.00**	**0.00**	**0.01**	**0.01**	**0.01**	**0.01**	**0.01**	**0.00**	**0.00**	**0.00**	**0.01**
Mg	**0.94**	**1.26**	**2.09**	**1.53**	**1.00**	**0.92**	**1.51**	**1.05**	**1.29**	**1.72**	**1.13**	**0.84**	**2.01**	**1.66**	**1.54**	**1.10**
Mn	**0.05**	**0.05**	**0.08**	**0.06**	**0.04**	**0.03**	**0.07**	**0.04**	**0.06**	**0.05**	**0.04**	**0.03**	**0.05**	**0.07**	**0.08**	**0.03**
Fe	**0.05**	**0.10**	**0.17**	**0.12**	**0.08**	**0.08**	**0.11**	**0.07**	**0.09**	**0.10**	**0.08**	**0.06**	**0.12**	**0.12**	**0.11**	**0.07**
K	**0.56**	**0.47**	**0.20**	**0.30**	**0.54**	**0.62**	**0.34**	**0.34**	**0.41**	**0.33**	**0.32**	**0.55**	**0.11**	**0.36**	**0.38**	**0.34**
Ca	**0.02**	**0.02**	**0.03**	**0.03**	**0.02**	**0.02**	**0.02**	**0.02**	**0.02**	**0.02**	**0.03**	**0.02**	**0.05**	**0.02**	**0.03**	**0.04**
Total (cation)	**7.04**	**7.14**	**7.37**	**7.13**	**7.06**	**7.06**	**7.16**	**6.96**	**7.11**	**7.26**	**6.98**	**7.01**	**7.21**	**7.24**	**7.19**	**6.98**
O (fixed)	**11**	**11**	**11**	**11**	**11**	**11**	**11**	**11**	**11**	**11**	**11**	**11**	**11**	**11**	**11**	**11**

Mineral	Illites								
analysis number	25 / 1 .	26 / 1 .	13 / 1 .	2 / 1 .	16 / 1 .	22 / 1 .	23 / 1 .	15	34 / 1 .
Element (%wt oxide)									
Al2O3	32.65	31.72	29.34	31.46	30.78	35.00	34.94	23.76	31.41
SiO2	48.10	47.53	46.90	48.16	48.63	50.51	49.31	51.97	45.63
TiO2	0.03	0.04	0.09	0.10	0.08	0.01	0.03	0.00	0.07
Na2O	0.16	0.14	0.09	0.08	0.08	0.19	0.22	0.00	0.06
MgO	4.44	4.97	4.95	4.97	4.32	0.97	1.06	0.84	3.74
MnO	0.29	0.34	0.27	0.26	0.21	0.03	0.02	0.00	0.19
FeO	0.61	0.73	0.70	0.63	0.87	0.22	0.27	7.93	0.45
K2O	6.17	6.93	7.42	9.07	8.42	7.59	6.64	4.89	7.85
CaO	0.29	0.24	0.21	0.13	0.17	0.19	0.32	0.00	0.19
Total	92.74	92.64	89.99	94.87	93.56	94.72	92.79	89.39	89.58
Structural formula									
Al	**2.55**	**2.50**	**2.39**	**2.45**	**2.42**	**2.67**	**2.71**	**1.96**	**2.57**
Si	**3.19**	**3.18**	**3.24**	**3.19**	**3.25**	**3.27**	**3.25**	**3.64**	**3.17**
Ti	**0.00**	**0.00**	**0.00**	**0.01**	**0.00**	**0.00**	**0.00**	**0.00**	**0.00**
Na	**0.02**	**0.02**	**0.01**	**0.01**	**0.01**	**0.02**	**0.03**	**0.00**	**0.01**
Mg	**0.44**	**0.50**	**0.51**	**0.49**	**0.43**	**0.09**	**0.10**	**0.09**	**0.39**
Mn	**0.02**	**0.02**	**0.02**	**0.01**	**0.01**	**0.00**	**0.00**	**0.00**	**0.01**
Fe	**0.03**	**0.04**	**0.04**	**0.03**	**0.05**	**0.01**	**0.01**	**0.46**	**0.03**
K	**0.52**	**0.59**	**0.65**	**0.77**	**0.72**	**0.63**	**0.56**	**0.44**	**0.70**
Ca	**0.02**	**0.02**	**0.02**	**0.01**	**0.01**	**0.01**	**0.02**	**0.00**	**0.01**
Total (cation)	**6.80**	**6.87**	**6.89**	**6.97**	**6.90**	**6.72**	**6.69**	**6.59**	**6.89**
O (fixed)	**11**	**11**	**11**	**11**	**11**	**11**	**11**	**11**	**11**

Mineral	Muscovite									
analysis number	3	4	5	18 / 1 .	30 / 1 .	33 / 1 .	6	10	12	14
Element (%wt oxide)										
Al2O3	28.59	28.94	29.31	32.44	33.19	32.43	28.69	28.75	28.52	29.35
SiO2	48.05	47.96	47.13	49.45	49.41	48.85	48.11	47.89	48.19	47.07
TiO2	0.06	0.01	0.09	0.04	0.07	0.10	0.05	0.07	0.07	0.12
Na2O	0.04	0.08	0.03	0.11	0.15	0.08	0.03	0.01	0.03	0.05
MgO	0.28	0.43	0.61	1.63	1.55	2.21	0.47	0.29	0.57	0.69
MnO	0.07	0.02	0.10	0.07	0.06	0.10	0.06	0.12	0.04	0.07
FeO	6.62	7.41	5.79	0.16	0.13	0.27	6.41	6.63	6.37	5.81
K2O	9.81	9.94	9.87	10.00	9.92	9.84	9.75	9.88	9.79	9.79
CaO	0.03	0.03	0.01	0.10	0.13	0.07	0.02	0.01	0.02	0.00
Total	93.55	94.82	92.94	93.99	94.60	93.96	93.59	93.65	93.60	92.95
Structural formula										
Al	**2.33**	**2.34**	**2.40**	**2.54**	**2.58**	**2.54**	**2.33**	**2.34**	**2.32**	**2.40**
Si	**3.32**	**3.29**	**3.27**	**3.29**	**3.26**	**3.25**	**3.32**	**3.31**	**3.33**	**3.27**
Ti	**0.00**	**0.00**	**0.00**	**0.00**	**0.00**	**0.00**	**0.00**	**0.00**	**0.00**	**0.01**
Na	**0.01**	**0.01**	**0.00**	**0.01**	**0.02**	**0.01**	**0.00**	**0.00**	**0.00**	**0.01**
Mg	**0.03**	**0.04**	**0.06**	**0.16**	**0.15**	**0.22**	**0.05**	**0.03**	**0.06**	**0.07**
Mn	**0.00**	**0.00**	**0.01**	**0.00**	**0.00**	**0.01**	**0.00**	**0.01**	**0.00**	**0.00**
Fe	**0.38**	**0.42**	**0.34**	**0.01**	**0.01**	**0.01**	**0.37**	**0.38**	**0.37**	**0.34**
K	**0.87**	**0.87**	**0.87**	**0.85**	**0.83**	**0.84**	**0.86**	**0.87**	**0.86**	**0.87**
Ca	**0.00**	**0.00**	**0.00**	**0.01**	**0.01**	**0.01**	**0.00**	**0.00**	**0.00**	**0.00**
Total (cation)	**6.94**	**6.98**	**6.96**	**6.87**	**6.87**	**6.89**	**6.94**	**6.95**	**6.94**	**6.96**
O (fixed)	**11**	**11**	**11**	**11**	**11**	**11**	**11**	**11**	**11**	**11**

662
663

Mineral	Chlorite												
analysis number	28 / 1 .	24 / 1 .	36 / 1 .	17 / 1 .	19 / 1 .	21 / 1 .	1	7	8	9	11	13	2
Element (%wt oxide)													
Al2O3	23.10	23.77	23.49	25.72	25.70	24.60	20.30	20.18	20.08	20.22	20.11	20.27	20.57
SiO2	34.37	35.21	37.94	38.83	37.86	37.62	27.01	25.45	25.66	25.51	25.69	25.53	27.32
TiO2	0.05	0.03	0.03	0.00	0.06	0.03	0.06	0.01	0.00	0.00	0.01	0.02	0.01
Na2O	0.03	0.01	0.04	0.02	0.03	0.02	0.00	0.05	0.19	0.00	0.04	0.02	0.00
MgO	19.42	22.40	20.90	18.26	18.53	22.26	16.50	13.94	13.73	13.65	13.71	13.95	16.71
MnO	1.15	1.27	1.05	0.97	1.09	1.24	0.33	0.30	0.37	0.23	0.34	0.26	0.29
FeO	2.29	2.41	2.30	1.94	2.03	2.29	22.48	24.36	27.85	26.98	27.91	27.82	23.64
K2O	0.18	0.24	0.76	0.29	0.28	0.31	0.00	0.00	0.00	0.00	0.00	0.00	0.00
CaO	0.51	0.38	0.55	0.62	0.55	0.41	0.10	0.00	0.00	0.00	0.00	0.00	0.09
Total	81.10	85.71	87.06	86.65	86.12	88.78	86.78	84.29	87.88	86.59	87.81	87.87	88.63
Structural formula													
Al	**2.68**	**2.62**	**2.54**	**2.76**	**2.78**	**2.05**	**2.50**	**2.60**	**2.53**	**2.57**	**2.53**	**2.55**	**2.49**
Si	**3.38**	**3.30**	**3.48**	**3.54**	**3.48**	**2.66**	**2.83**	**2.78**	**2.74**	**2.75**	**2.74**	**2.72**	**2.81**
Ti	**0.00**	**0.00**	**0.00**	**0.00**	**0.00**	**0.00**	**0.00**	**0.00**	**0.00**	**0.00**	**0.00**	**0.00**	**0.00**
Na	**0.01**	**0.00**	**0.01**	**0.00**	**0.00**	**0.00**	**0.00**	**0.01**	**0.04**	**0.00**	**0.01**	**0.00**	**0.00**
Mg	**2.85**	**3.13**	**2.86**	**2.48**	**2.54**	**2.35**	**2.57**	**2.27**	**2.19**	**2.19**	**2.18**	**2.22**	**2.56**
Mn	**0.10**	**0.10**	**0.08**	**0.07**	**0.08**	**0.07**	**0.03**	**0.03**	**0.03**	**0.02**	**0.03**	**0.02**	**0.03**
Fe	**0.19**	**0.19**	**0.18**	**0.15**	**0.16**	**0.14**	**1.97**	**2.23**	**2.49**	**2.43**	**2.49**	**2.48**	**2.03**
K	**0.02**	**0.03**	**0.09**	**0.03**	**0.03**	**0.03**	**0.00**	**0.00**	**0.00**	**0.00**	**0.00**	**0.00**	**0.00**
Ca	**0.05**	**0.04**	**0.05**	**0.06**	**0.05**	**0.03**	**0.01**	**0.00**	**0.00**	**0.00**	**0.00**	**0.00**	**0.01**
Total (cation)	**9.29**	**9.40**	**9.29**	**9.10**	**9.14**	**7.33**	**9.92**	**9.92**	**10.02**	**9.97**	**9.99**	**10.00**	**9.94**
O (fixed)	**14**	**14**	**14**	**14**	**14**	**14**	**14**	**14**	**14**	**14**	**14**	**14**	**14**

664
665

Table A.2 – XRD pattern decomposition

Sample	Position	Intensity	Area	FWHM	Interpretation
16STH19-1_AD 315-500 µm	5.81	10900.6	13177.4	1.14	Chlorite-Smectite (001)
	6.12	6828.17	1946.31	0.27	
	6.69	1939.5	195.95	0.15	Illite-Smectite [Illite-rich] ?
	8.67	2200.51	1229.94	0.53	Illite (001)
	8.80	3695.56	466.4	0.12	Mica (001)
	12.34	8267.05	2970.77	0.34	Chlorite (002)
	13.76	1294.95	353.38	0.26	Feldspar
	17.68	3442.68	1164.31	0.32	Illite-Mica (002)
	18.64	3529.18	1370.53	0.36	Chlorite (003)
16STH19-1_EG 315-500 µm	5.14	6569.07	4575.52	0.65	Smectite (001)
	6.09	5696.10	2019.63	0.33	Chlorite (001)
	8.72	1406.39	1054.28	0.7	Illite (001)
	8.8	3104.77	476.93	0.14	Mica (001)
	9.52	627.18	125.44	0.38	Smectite (002)
	12.25	3449.96	1846.5	0.5	Chlorite (002) [Chlorite-Smectite]
	12.37	3058.74	665.46	0.2	Chlorite (002) [Chlorite]
	13.81	986.34	186.23	0.18	Feldspar
	17.68	1393.94	388.12	0.26	Illite-Mica (002)
	18.65	2294.22	1024.21	0.42	Chlorite (003)

Table A.3 – Compiled Ar-Ar results ***[Supplemental file: Excel files]***

	K-Ar total fusion (Ma)	2σ	Plateau age (Ma)	2σ	MSWD	$\%^{39}Ar$ released	Isochron age (Ma)	2σ	$^{40}Ar/^{36}Ar$ i	2σ
315 - 500 µm fraction										
Experiments:										
#B7-B8	2.53	0.32	2.78	0.22	0.31	98%	2.77	0.33	299.9	12.6
#A9 A10	2.27	0.75	2.45	0.25	0.38	87%	2.59	0.31	292.6	9
#B12	2.57	0.25	2.62	0.2	0.33	99%	2.57	0.31	297.4	8.5
#B2	2.52	0.62	2.55	0.44	0.32	61%	2.88	1.54	277.2	109
Combined experiments	2.45	0.27	2.59	0.12	0.39	90%	2.67	0.17	295.9	5.5

9. References

AREHART, G.., CHRISTENSON, B.., WOOD, C.., FOLAND, K.., & BROWNE, P.R.. **2002**. Timing of volcanic, plutonic and geothermal activity at Ngatamariki, New Zealand. *Journal of Volcanology and Geothermal Research*, 116, 201–214, doi: 10.1016/S0377-0273(01)00315-8.

ÁRKAI, P. **1991**. Chlorite crystallinity: an empirical approach and correlation with illite crystallinity, coal rank and mineral facies as exemplified by Palaeozoic and Mesozoic rocks of northeast Hungary. *Journal of Metamorphic Geology*, 9, 723–734, doi: 10.1111/j.1525-1314.1991.tb00561.x.

ARNÓRSSON, S. **1995**. Geothermal systems in Iceland: Structure and conceptual models—I. High-temperature areas. *Geothermics*, 24, 561–602, doi: 10.1016/0375-6505(95)00025-9.

BARCELONA, H., YAGUPSKY, D., VIGIDE, N., & SENGER, M. **2019**. Structural model and slip-dilation tendency analysis at the Copahue geothermal system: Inferences on the reservoir geometry. *Journal of Volcanology and Geothermal Research*, 375, 18–31, doi: 10.1016/j.jvolgeores.2019.03.007.

BARNES, H.L. **1997**. *Geochemistry of Hydrothermal Ore Deposits*. John Wiley & Sons.

BEAUCHAMPS, G., LEDÉSERT, B., HÉBERT, R., NAVELOT, V., & FAVIER, A. **2019**. The characterisation of an exhumed high temperature paleo geothermal system on Terre de Haut Island (the Les Saintes archipelago , Guadeloupe) in terms of clay minerals and petrophysics. *Geothermal Energy*, 1–18, doi: 10.1186/s40517-019-0122-y.

BERTANI, R. **2016**. Geothermal power generation in the world 2010–2014 update report. *Geothermics*, 60, 31–43, doi: 10.1016/j.geothermics.2015.11.003.

BIBBY, H.M., CALDWELL, T.G., DAVEY, F.J., & WEBB, T.H. **1995**. Geophysical evidence on the structure of the Taupo Volcanic Zone and its hydrothermal circulation. *Journal of Volcanology and Geothermal Research*, 68, 29–58, doi: 10.1016/0377-0273(95)00007-H.

BOUYSSE, P. & WESTERCAMP, D. **1990**. Subduction of Atlantic aseismic ridges and Late Cenozoic evolution of the Lesser Antilles island arc. *Tectonophysics*, 175, 349–380, doi: 10.1016/0040-1951(90)90180-G.

BROCKAMP, O., CLAUER, N., & ZUTHER, M. **2003**. Authigenic sericite record of a fossil geothermal system: the Offenburg trough, central Black Forest, Germany. *International Journal of Earth Sciences*, 92, 843–851, doi: 10.1007/s00531-003-0368-1.

BROWNE, P.R.L. **1978**. Hydrothermal alteration in active geothermal fields. *Annual Review of Earth and Planetary Sciences*, 6, 229–250.

CARICCHI, L., ANNEN, C., RUST, A., & BLUNDY, J. **2012**. Insights into the mechanisms and timescales of pluton assembly from deformation patterns of mafic enclaves. *Journal of Geophysical Research: Solid Earth*, 117, n/a-n/a, doi: 10.1029/2012JB009325.

CARLUT, J., QUIDELLEUR, X., COURTILLOT, V., & BOUDON, G. **2000**. Paleomagnetic directions and K/Ar dating of 0 to 1 Ma lava flows from La Guadeloupe Island (French West Indies): Implications for time-averaged field models. *Journal of Geophysical Research: Solid Earth*, 105, 835–849, doi: 10.1029/1999JB900238.

CARSLAW, H.S. & JAEGER, J.C. **1959**. *Conduction of Heat in Solids*. London, Oxford Univ. Press.

CHERKOSE, B.A. & MIZUNAGA, H. **2018**. Resistivity imaging of Aluto-Langano geothermal field using 3-D magnetotelluric inversion. *Journal of African Earth*

Sciences, 139, 307–318, doi: 10.1016/j.jafrearsci.2017.12.017.
CLAUER, N. **2013**. The K-Ar and 40Ar/39Ar methods revisited for dating fine-grained K-bearing clay minerals. *Chemical Geology*, 354, 163–185, doi: 10.1016/j.chemgeo.2013.05.030.
CLAUER, N., ZWINGMANN, H., LIEWIG, N., & WENDLING, R. **2012**. Comparative 40Ar/39Ar and K–Ar dating of illite-type clay minerals: A tentative explanation for age identities and differences. *Earth-Science Reviews*, 115, 76–96, doi: 10.1016/j.earscirev.2012.07.003.
DALRYMPLE, G.B., GROVE, M., LOVERA, O.M., HARRISON, T.M., HULEN, J.B., & LANPHERE, M.A. **1999**. Age and thermal history of the Geysers plutonic complex (felsite unit), Geysers geothermal field, California: a 40Ar/39Ar and U–Pb study. *Earth and Planetary Science Letters*, 173, 285–298, doi: 10.1016/S0012-821X(99)00223-X.
DELANEY, P.T. **1982**. Rapid intrusion of magma into wet rock: Groundwater flow due to pore pressure increases. *Journal of Geophysical Research: Solid Earth*, 87, 7739–7756.
DELOULE, E. & TURCOTTE, D.L. **1989**. The flow of hot brines in cracks and the formation of ore deposits. *Economic Geology*, 84, 2217–2225, doi: doi: 10.2113/gsecongeo.84.8.2217.
DONG, H., HALL, C.M., PEACOR, D.R., & HALLIDAY, A.N. **1995**. Mechanisms of Argon Retention in Clays Revealed by Laser 40Ar-39Ar Dating. *Science*, 267, 355–359, doi: 10.1126/science.267.5196.355.
DRITS, V., SRODON, J., & EBERL, D.D. **1997**. XRD Measurement of Mean Crystallite Thickness of Illite and Illite/Smectite: Reappraisal of the Kubler Index and the Scherrer Equation. *Clays and Clay Minerals*, 45, 461–475, doi: 10.1346/CCMN.1997.0450315.
ELDURSI, K., BRANQUET, Y., GUILLOU-FROTTIER, L., & MARCOUX, E. **2009**. Numerical investigation of transient hydrothermal processes around intrusions: Heat-transfer and fluid-circulation controlled mineralization patterns. *Earth and Planetary Science Letters*, 288, 70–83, doi: 10.1016/j.epsl.2009.09.009.

FAURE, G. **1986**. *Principles of Isotope Geology*. New-York, John Wiley & Sons.
FAVIER, A. **2019**. *Evolution Spatio-Temporelle de l'hydrothermalisme Dans La Plaque Supérieure de l'arc Des Petites Antilles En Guadeloupe. Applications Aux Systèmes Géothermaux.* Université des Antilles, Pointe-à-Pitre, Guadeloupe.
FAVIER, A., LARDEAUX, J.-M., LEGENDRE, L., VERATI, C., PHILIPPON, M., CORSINI, M., MÜNCH, P., & VENTALON, S. **2019**. Tectono-metamorphic evolution of shallow crustal levels within active volcanic arcs. Insights from the exhumed Basal Complex of Basse-Terre (Guadeloupe, French West Indies). *BSGF - Earth Sciences Bulletin*, 190, 22, doi: 10.1051/bsgf/2019011.
FAVIER, A., LARDEAUX, J.-M., CORSINI, M., VERATI, C., NAVELOT, V., GERAUD, Y., DIRAISON, M., VENTALON, S., & VOITUS, E. **2021**. Characterization of an exhumed high-temperature hydrothermal system and its application for deep geothermal exploration: An example from Terre-de-Haut Island (Guadeloupe archipelago, Lesser Antilles volcanic arc). *Journal of Volcanology and Geothermal Research*, 107256, doi: 10.1016/j.jvolgeores.2021.107256.

GOLDFARB, R.., GROVES, D.., & GARDOLL, S. **2001**. Orogenic gold and geologic time: a global synthesis. *Ore Geology Reviews*, 18, 1–75, doi: 10.1016/S0169-1368(01)00016-6.
GRIMES, S., RICKARD, D., HAWKESWORTH, C., VAN CALSTEREN, P., & BROWNE, P. **1998**.

A U–Th calcite isochron age from an active geothermal field in New Zealand. *Journal of Volcanology and Geothermal Research*, 81, 327–333, doi: 10.1016/S0377-0273(98)00005-5.

GROVES, D.., GOLDFARB, R.., GEBRE-MARIAM, M., HAGEMANN, S.., & ROBERT, F. **1998**. Orogenic gold deposits: A proposed classification in the context of their crustal distribution and relationship to other gold deposit types. *Ore Geology Reviews*, 13, 7–27, doi: 10.1016/s0169-1368(97)00012-7.

GUILBERT, J.M. & PARK, C.F.J. **1986**. *The Geology of Ore Deposits*. New York, W. H. Freeman and Compagny.

HAINES, S.H. & VAN DER PLUIJM, B.A. **2008**. Clay quantification and Ar–Ar dating of synthetic and natural gouge: Application to the Miocene Sierra Mazatán detachment fault, Sonora, Mexico. *Journal of Structural Geology*, 30, 525–538, doi: 10.1016/j.jsg.2007.11.012.

HALL, C.M., HIGUERAS, P.L., KESLER, S.E., LUNAR, R., DONG, H., & HALLIDAY, A.N. **1997**. Dating of alteration episodes related to mercury mineralization in the Almadén district, Spain. *Earth and Planetary Science Letters*, 148, 287–298, doi: 10.1016/S0012-821X(97)00041-1.

HAMES, W., UNGER, D., SAUNDERS, J., & KAMENOV, G. **2009**. Early Yellowstone hotspot magmatism and gold metallogeny. *Journal of Volcanology and Geothermal Research*, 188, 214–224, doi: 10.1016/j.jvolgeores.2009.07.020.

HEDENQUIST, J.W. & BROWNE, P.R.L. **1989**. The evolution of the Waiotapu geothermal system, New Zealand, based on the chemical and isotopic composition of its fluids, minerals and rocks. *Geochimica et Cosmochimica Acta*, 53, 2235–2257, doi: 10.1016/0016-7037(89)90347-5.

HEDENQUIST, J.W., ARRIBAS, A.J., & GONZALEZ-URIEN, E. **2000**. Exploration for epithermal gold deposits. *In*: *SEG Review*. 245–277.

HENLEY, R.W. & ELLIS, A.J. **1983**. Geothermal systems ancient and modern: a geochemical review. *Earth-Science Reviews*, 19, 1–50, doi: 10.1016/0012-8252(83)90075-2.

HOINKES, C., HAUZENBERGER, C.A., & SCHMID, R. **2005**. Metamorphic rocks - Classification, nomenclature and formation. *In*: Selley, R. C., Cocks, R. & Plimer, I. R. (eds) *Encyclopedia of Geology*. Academic Press, 386–402.

HOWARD, S.A. & PRESTON, K.D. **1989**. Profile fitting of powder diffraction patterns. *In*: *Modern Powder Diffraction*. 217–275.

INOUE, A. & KITAGAWA, R. **1994**. Morphological characteristics of illite clay minerals from a hydrothermal system. *American Mineralogist*, 79, 700–711.

INOUE, A., UTADA, M., & WAKITA, K. **1992**. Smectite-to-illite conversion in natural hydrothermal systems. *Applied Clay Science*, 7, 131–145, doi: 10.1016/0169-1317(92)90035-L.

ISIK, V., UYSAL, I.T., CAGLAYAN, A., & SEYITOGLU, G. **2014**. The evolution of intraplate fault systems in central Turkey: Structural evidence and Ar-Ar and Rb-Sr age constraints for the Savcili Fault Zone. *Tectonics*, 33, 1875–1899, doi: 10.1002/2014TC003565.

JACQUES, D. & MAURY, R.C. **1988**. Carte géologique au 1/20 000e, département de la Guadeloupe, Les Saintes. *BRGM, Service Géologique National, Orléans*.

JACQUES, D., MAURY, R.C., & BELLON, H. **1984**. *Geology and K-Ar geochronology of Les Saintes island, guadeloupe, Frend West-Indies Géologie et géochronologie 40K-40Ar des îles des Saintes (Guadeloupe)*. Gauthier-Villars.

JAEGER, J.C. **1959**. Temperatures outside a cooling intrusive sheet. *American Journal of Science*, 257, 44–54, doi: 10.2475/ajs.257.1.44.

820 JAEGER, J.C. **1968**. Cooling and solidification of igneous rocks. *In*: Hess, H. H. &
821 Poldervaart, A. (eds) *Basalts – The Poldervaart Treatise on Rocks of Basaltic*
822 *Composition, Vol.2*. New-York, John Wiley, 503–536.

823 JI, J. & BROWNE, P.R.L. **2000**. Relationship between illite crystallinity and temperature
824 in active geothermal systems of New Zealand. *Clays and Clay Minerals*, 48,
825 139–144.
826 JOURDAN, F., MATZEL, J.P., & RENNE, P.R. **2007**. 39Ar and 37Ar recoil loss during
827 neutron irradiation of sanidine and plagioclase. *Geochimica et Cosmochimica*
828 *Acta*, 71, 2791–2808, doi: 10.1016/j.gca.2007.03.017.
829 KISSLING, W.M. **1999**. Modeling of cooling plutons in the Taupo Volcanic Zone New
830 Zealand. *In*: *24th Workshop on Geothermal Reservoir Engineering*. Stanford,
831 California, SGP-TR-162.

832 KOPPERS, A.A.P. **2002**. ArArCALC—software for 40Ar/39Ar age calculations.
833 *Computers & Geosciences*, 28, 605–619, doi: 10.1016/S0098-3004(01)00095-4.
834 KÜBLER, B. **1967**. La cristallinité de l`illite et les zones tout à fait supérieures du
835 métamorphisme. *In*: *Étages Tectoniques, Colloque de Neuchâtel 1966*. La
836 Baconniere, Neuchâte, 105–121.
837 LEE, J.-Y., MARTI, K., SEVERINGHAUS, J.P., KAWAMURA, K., H-S., Y., LEE, J.B., & KIM,
838 J.S. **2006**. A redetermination of the isotopic abundances of atmospheric Ar.
839 *Geochimica et Cosmochimica Acta*, 4507–4512.
840 MÁRTON, I., MORITZ, R., & SPIKINGS, R. **2010**. Application of low-temperature
841 thermochronology to hydrothermal ore deposits: Formation, preservation and
842 exhumation of epithermal gold systems from the Eastern Rhodopes, Bulgaria.
843 *Tectonophysics*, 483, 240–254, doi: 10.1016/j.tecto.2009.10.020.
844 MERRIMAN, R.J. & PEACOR, D.R. **1998**. Very Low-Grade Metapelites: Mineralogy,
845 Microfabrics and Measuring Reaction Progress. *In*: *Low-Grade Metamorphism*.
846 Oxford, UK, Blackwell Publishing Ltd., 10–60., doi:
847 10.1002/9781444313345.ch2.
848 MEYER, C. & HEMLEY, J.J. **1967**. Wall rock alteration. *In*: *Geochemistry of*
849 *Hydrothermal Ore Deposits*. New-York, 166–235.
850 MILICICH, S.D., CHAMBEFORT, I., WILSON, C.J.N., ALCARAZ, S., IRELAND, T.R.,
851 BARDSLEY, C., & SIMPSON, M.P. **2020**. A zircon U-Pb geochronology for the
852 Rotokawa geothermal system, New Zealand, with implications for Taupō
853 Volcanic Zone evolution. *Journal of Volcanology and Geothermal Research*, 389,
854 106729, doi: 10.1016/j.jvolgeores.2019.106729.
855 NAKAI, S., HALLIDAY, A.N., KESLER, S.E., JONES, H.D., KYLE, J.R., & LANE, T.E. **1993**.
856 Rb-Sr dating of sphalerites from Mississippi Valley-type (MVT) ore deposits.
857 *Geochimica et Cosmochimica Acta*, 57, 417–427, doi: 10.1016/0016-
858 7037(93)90440-8.
859 NAVELOT, V., GERAUD, Y., FAVIER, A., DIRAISON, M., CORSINI, M., LARDEAUX, J.-M.,
860 VERATI, C., MERCIER DE LEPINAY, J., LEGENDRE, L., & BEAUCHAMPS, G. **2018**.
861 Petrophysical properties of volcanic rocks and impacts of hydrothermal alteration
862 in the Guadeloupe Archipelago (West Indies). *Journal of Volcanology and*
863 *Geothermal Research*, 360, 1–21, doi: 10.1016/j.jvolgeores.2018.07.004.
864 OLIVEROS, VER., AGUIRRE, L., MORATA, D., SIMONETTI, A., VERGARA, M., BELMAR, M., &
865 CALDERÓN, S. **2008**. Geochronology of very low-grade Mesozoic Andean
866 metabasites; an approach through the K–Ar, 40 Ar/ 39 Ar and U–Pb LA-MC-ICP-
867 MS methods. *Journal of the Geological Society*, 165, 579–584, doi:
868 10.1144/0016-76492007-113.

869 OZE, C., CATTELL, H., & GROVE, M. **2017**. 40 Ar/ 39 Ar dating and thermal modeling of
870 adularia to constrain the timing of hydrothermal activity in magmatic settings.
871 *Geology*, 45, 43–46, doi: 10.1130/G38405.1.
872 RAGNARSSON, A. **2015**. Geothermal development in Iceland 2010–2014. *In*:
873 *Proceedings World Geothermal Congress 2015*. Melbourne, Australia, 15.
874 RENNE, P.R., MUNDIL, R., BALCO, G., MIN, K., & LUDWIG, K.R. **2010**. Joint
875 determination of 40K decay constants and 40Ar∗/40K for the Fish Canyon
876 sanidine standard, and improved accuracy for 40Ar/39Ar geochronology.
877 *Geochimica et Cosmochimica Acta*, 74, 5349–5367, doi:
878 10.1016/j.gca.2010.06.017.
879 RICCI, J., LAHITTE, P., & QUIDELLEUR, X. **2015a**. Construction and destruction rates of
880 volcanoes within tropical environment: Examples from the Basse-Terre Island
881 (Guadeloupe, Lesser Antilles). *Geomorphology*, 228, 597–607, doi:
882 10.1016/j.geomorph.2014.10.002.

883 RICCI, J., QUIDELLEUR, X., & LAHITTE, P. **2015b**. Volcanic evolution of central Basse-
884 Terre Island revisited on the basis of new geochronology and geomorphology
885 data. *Bulletin of Volcanology*, 77, 84, doi: 10.1007/s00445-015-0970-7.

886 RICCI, J., QUIDELLEUR, X., PALLARES, C., & LAHITTE, P. **2017**. High-resolution K-Ar
887 dating of a complex magmatic system: The example of Basse-Terre Island
888 (French West Indies). *Journal of Volcanology and Geothermal Research*, 345,
889 142–160, doi: 10.1016/j.jvolgeores.2017.07.013.

890 ROSENBERG, M.D., WILSON, C.J.N., BIGNALL, G., IRELAND, T.R., SEPULVEDA, F., &
891 CHARLIER, B.L.A. **2020**. Structure and evolution of the Wairakei–Tauhara
892 geothermal system (Taupo Volcanic Zone, New Zealand) revisited with a new
893 zircon geochronology. *Journal of Volcanology and Geothermal Research*, 390,
894 106705, doi: 10.1016/j.jvolgeores.2019.106705.
895 ROWLAND, J. V. & SIBSON, R.H. **2004**. Structural controls on hydrothermal flow in a
896 segmented rift system, Taupo Volcanic Zone, New Zealand. *Geofluids*, 4, 259–
897 283, doi: 10.1111/j.1468-8123.2004.00091.x.
898 SAMPER, A., QUIDELLEUR, X., LAHITTE, P., & MOLLEX, D. **2007**. Timing of effusive
899 volcanism and collapse events within an oceanic arc island: Basse-Terre,
900 Guadeloupe archipelago (Lesser Antilles Arc). *Earth and Planetary Science*
901 *Letters*, 258, 175–191, doi: 10.1016/j.epsl.2007.03.030.
902 SAMPER, A., QUIDELLEUR, X., KOMOROWSKI, J.-C., LAHITTE, P., & BOUDON, G. **2009**.
903 Effusive history of the Grande Découverte Volcanic Complex, southern Basse-
904 Terre (Guadeloupe, French West Indies) from new K–Ar Cassignol–Gillot ages.
905 *Journal of Volcanology and Geothermal Research*, 187, 117–130, doi:
906 10.1016/j.jvolgeores.2009.08.016.
907 SASADA, M., TAGUCHI, S., & HEDENQUIST, J.W. **2000**. Japanese geothermal systems
908 developments in the 1990s-Preface. *Geothermics*, 29, 123–126.
909 STEIGER, R.H. & JÄGER, E. **1977**. Subcommission on geochronology: Convention on
910 the use of decay constants in geo- and cosmochronology. *Earth and Planetary*
911 *Science Letters*, 36, 359–362, doi: 10.1016/0012-821X(77)90060-7.
912 VELADOR, J.M., HEIZLER, M.T., & CAMPBELL, A.R. **2010**. Timing of Magmatic Activity
913 and Mineralization and Evidence of a Long-Lived Hydrothermal System in the
914 Fresnillo Silver District, Mexico: Constraints from 40ar/39Ar Geochronology.
915 *Economic Geology*, 105, 1335–1349, doi: 10.2113/econgeo.105.7.1335.

916 VELDE, B. **1985**. *A Physico-Chemical Explanation of Their Occurrence.*

Developments in Sedimentology. Amsterdam, Elsevier.
VERATI, C. & JOURDAN, F. **2014**. Modelling effect of sericitization of plagioclase on the 40 K/ 40 Ar and 40 Ar/ 39 Ar chronometers: implication for dating basaltic rocks and mineral deposits. *Geological Society, London, Special Publications*, 378, 155–174, doi: 10.1144/SP378.14.
VERATI, C., PATRIER-MAS, P., LARDEAUX, J.-M., & BOUCHOT, V. **2014**. Timing of geothermal activity in an active island-arc volcanic setting: First 40Ar/39Ar dating from Bouillante geothermal field (Guadeloupe, French West Indies). *Geological Society, London, Special Publications*, 378, 285–295, doi: 10.1144/SP378.19.
VERATI, C., MAZABRAUD, Y., LARDEAUX, J.-M., CORSINI, M., SCHNEIDER, D., VOITUS, E., & ZAMI, F. **2016**. Tectonic evolution of Les Saintes archipelago (Guadeloupe, French West Indies): relation with the Lesser Antilles arc system. *Bulletin de la Société Géologique de France*, 187, 3–10, doi: 10.2113/gssgfbull.187.1.3.
VILLA, I.M., RUGGIERI, G., PUXEDDU, M., & BERTINI, G. **2006**. Geochronology and isotope transport systematics in a subsurface granite from the Larderello–Travale geothermal system (Italy). *Journal of Volcanology and Geothermal Research*, 152, 20–50, doi: 10.1016/j.jvolgeores.2005.09.011.
WARR, L.N. & COX, S.C. **2016**. Correlating illite (Kübler) and chlorite (Árkai) "crystallinity" indices with metamorphic mineral zones of the South Island, New Zealand. *Applied Clay Science*, 134, 164–174, doi: 10.1016/j.clay.2016.06.024.
WHITE, N.C. & HEDENQUIST, J.W. **1990**. Epithermal environments and styles of mineralization: Variations and their causes, and guidelines for exploration. *Journal of Geochemical Exploration*, 36, 445–474, doi: 10.1016/0375-6742(90)90063-G.
WIEWIÓRA, A. & WEISS, Z. **1990**. Crystallochemical classifications of phyllosilicates based on the unified system of projection of chemical composition: II. The chlorite group. *Clay Minerals*, 25, 83–92, doi: 10.1180/claymin.1990.025.1.09.
WILSON, C.J.N., CHARLIER, B.L.A., FAGAN, C.J., SPINKS, K.D., GRAVLEY, D.M., SIMMONS, S.F., & BROWNE, P.R.L. **2008**. U–Pb dating of zircon in hydrothermally altered rocks as a correlation tool: Application to the Mangakino geothermal field, New Zealand. *Journal of Volcanology and Geothermal Research*, 176, 191–198, doi: 10.1016/j.jvolgeores.2008.04.010.
WOJDYR, M. **2010**. Fityk : a general-purpose peak fitting program. *Journal of Applied Crystallography*, 43, 1126–1128, doi: 10.1107/S0021889810030499.
WOLDEGABRIEL, G., BROXTON, D.E., & BYERS, F.M. **1996**. Mineralogy and temporal relations of coexisting authigenic minerals in altered silicic tuffs and their utility as potential low-temperature dateable minerals. *Journal of Volcanology and Geothermal Research*, 71, 155–165, doi: 10.1016/0377-0273(95)00064-X.
ZAMI, F., QUIDELLEUR, X., RICCI, J., LEBRUN, J.-F., & SAMPER, A. **2014**. Initial sub-aerial volcanic activity along the central Lesser Antilles inner arc: New K–Ar ages from Les Saintes volcanoes. *Journal of Volcanology and Geothermal Research*, 287, 12–21, doi: 10.1016/j.jvolgeores.2014.09.011.